

A quantitative study of the interaction of two Richtmyer–Meshkov-unstable gas cylinders

C. Tomkins, K. Prestridge, P. Rightley, and M. Marr-Lyon

Dynamic Experimentation Division, Los Alamos National Laboratory, Los Alamos, New Mexico 87545

P. Vorobieff

Department of Mechanical Engineering, University of New Mexico, Albuquerque, New Mexico 87131

R. Benjamin

Dynamic Experimentation Division, Los Alamos National Laboratory, Los Alamos, New Mexico 87545

(Received 6 August 2002; accepted 30 December 2002; published 4 March 2003)

We experimentally investigate the evolution and interaction of two Richtmyer–Meshkov-unstable gas cylinders using concentration field visualization and particle image velocimetry. The heavy-gas (SF_6) cylinders have an initial spanwise separation of S/D (where D is the cylinder diameter) and are simultaneously impacted by a planar, Mach 1.2 shock. The resulting flow morphologies are highly reproducible and highly sensitive to the initial separation, which is varied from $S/D \approx 1.2$ to 2.0. The effects of the cylinder–cylinder interaction are quantified using both visualization and high-resolution velocimetry. Vorticity fields reveal that a principal interaction effect is the weakening of the inner vortices of the system. We observe a nonlinear, threshold-type behavior of inner vortex formation around $S/D = 1.5$. A correlation-based ensemble-averaging procedure extracts the persistent character of the unstable flow structures, and permits decomposition of the concentration fields into mean (deterministic) and fluctuating (stochastic) components. © 2003 American Institute of Physics. [DOI: 10.1063/1.1555802]

I. INTRODUCTION

The Richtmyer–Meshkov (RM) instability (Meshkov,¹ Richtmyer²) occurs during the impulsive acceleration of material interfaces in which the density gradient and pressure gradient are misaligned. This misalignment leads to a baroclinic deposition of vorticity that distorts the interface, leading to mixing and transition to turbulence at late time. RM instability has applications in a wide range of areas; three prominent examples are inertial confinement fusion (Lindl *et al.*³), astrophysics (Arnett *et al.*⁴), and supersonic combustion (Yang *et al.*⁵).

Most research in RM instability has focused on a perturbed single interface, the simplest example of which is a sinusoidal initial condition (e.g., Jacobs and Sheeley;⁶ Jones and Jacobs;⁷ Sadot *et al.*⁸). A slightly more complex extension of this is a layer or “curtain” of gas that results in a perturbed double interface (Jacobs *et al.*;⁹ Rightley *et al.*;^{10,11} Prestridge *et al.*^{12,13}). For a current review of the RM instability the reader is referred to the recent article by Brouillette¹⁴ and the more specific but complementary article by Zabusky,¹⁵ which emphasizes the role of coherent structures in the flow.

One simple test problem of recent interest is a shock wave interacting with a cylindrical (or circular, in two dimensions) fluid interface. This problem has been studied analytically in terms of vorticity deposition (Samtaney and Zabusky;¹⁶ Picone and Boris¹⁷), computationally (Yang *et al.*;⁵ Quirk and Karni;¹⁸ Zoldi¹⁹), and experimentally (Haas and Sturtevant;²⁰ Jacobs;²¹ Prestridge *et al.*²²). In this configuration, experiments and simulations show that the in-

terface enters a regime of nonlinear growth immediately, and the flow is soon dominated by a counter-rotating vortex pair, which evolves from the opposite-sign vorticity that is baroclinically deposited along opposing edges of the cylinder. At later time, waviness appears along the interface with a characteristic length scale much less than that associated with the primary instability. This waviness is typically interpreted as a manifestation of a secondary instability, possibly associated with Kelvin–Helmholtz shear instability, or possibly baroclinic in nature (Cook and Miller;²³ Zabusky²⁴). Eventually, the combination of instabilities will transition the flow to a state of incipient turbulence.

Experimentally, investigation of RM instability remains a challenge, although over the last decade or so there have been significant advancements in the field. In terms of improving the ideality of the instability, experiments with a membraneless interface between diffuse gases were first performed by Brouillette and Sturtevant,^{25,26} and this improvement has been refined by several others since that time (e.g., Bonazza and Sturtevant;²⁷ Jones and Jacobs⁷). In terms of improving the diagnostic, laser-sheet visualization of the flowfield has proven quite effective (e.g., Jacobs *et al.*;²⁸ Budzinski *et al.*²⁹), and, like the membraneless interface, this technique is now commonly employed.

In the current body of work on RM instability, however, quantitative experimental measurements are scarce. In particular, high-resolution, quantitative estimates of velocity/vorticity fields are almost nonexistent—even though the deposited vorticity is the principal mechanism driving the

instability. This scarcity is both a consequence of and a testament to the difficulty of performing planar, quantitative velocity measurements in a shock-accelerated flow. Another important and challenging issue in RM research is experimental repeatability. The sensitivity of the flow evolution to the initial conditions is well known, and often manifest as scatter in experimental data. As a result, highly repeatable experiments are the exception rather than the rule. In the present experiment, we aim to address these key voids in experimental RM research.

We report high-resolution, quantitative concentration and velocity/vorticity measurements of a highly repeatable experiment. The evolution and interaction of two shock-accelerated, heavy-gas cylinders are investigated, as an extension of the single-cylinder problem. (Visualization results on the double-cylinder problem were first reported in Tomkins *et al.*,³⁰ with qualitative analysis.) The cylinders are initially separated spanwise with nominal center-to-center spacing S/D , where D is the cylinder diameter, and impacted with a planar, Mach 1.2 shock wave. The initial spacing is incrementally varied from $S/D \approx 1.2$ to 2.0. Like the single-cylinder case, the double-cylinder problem has a simple initial geometry however, varying the initial cylinder spacing reveals highly complex behavior on both the large and small scales of the flow. The problem is interesting both from a shock–gas interaction standpoint—the shock wave must refract differently for each spacing as it passes through the structures—and from a vortex dynamics standpoint, as the post-shock flow involves the interaction of two to four vortex columns. The evolution of the flow structures is captured immediately before shock impact and at six times after shock impact using concentration-field visualization. In an independent set of experiments, particle image velocimetry (PIV) is used to capture the velocity field in the streamwise–spanwise plane at one (late) time, with the highest experimental resolution reported to date. The visualization and velocity results are linked by the high repeatability of the experiment.

The visualizations reveal that the flow morphologies are highly sensitive to the initial cylinder spacing, and hence, the degree of interaction between the cylinders. We quantify the effects of this interaction in terms of the concentration and vorticity fields, and introduce a new, rotationally invariant measure of mixing-zone width. These quantitative results show that the innermost vortex associated with each cylinder becomes increasingly weak as the cylinder spacing is reduced, and idealized simulations that incorporate this attenuation yield flow patterns that match the experimental data at all spacings studied. We also introduce a correlation-based ensemble-averaging technique, which extracts the persistent character of the unstable structures. The technique yields the first meaningful ensemble averages obtained on a shock-accelerated, unstable flow, and confirms the repeatability of the experiment. The concentration fields are decomposed into mean and fluctuating components, permitting calculation of the rms concentration fluctuations, which provides a quantitative measure of the sensitivity to initial conditions.

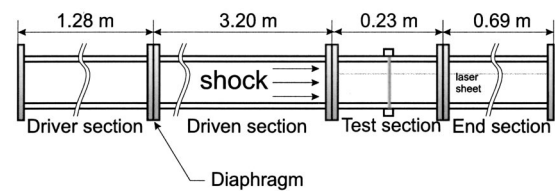


FIG. 1. Side-view schematic of shock tube.

II. EXPERIMENT

A. Experimental facility

A side-view schematic of the shock tube is presented in Fig. 1. The shock is generated by placing a diaphragm at the downstream end of the driver section, and pressurizing the section to 20 psig. Solenoid-driven blades puncture the diaphragm, releasing a Mach 1.2 shock in air, which becomes planar as it propagates through the driven section and impacts one or two cylinders of heavy gas in the test section. The heavy gas is sulfur hexafluoride, SF_6 , with a density five times that of air. The tube cross-section is 75 mm \times 75 mm.

A schematic of the test section is shown in Fig. 2. The gas cylinders are created as follows. Heavy gas is fed into a container that is elevated above the test section. Glycol/water fog droplets (nominally 0.5 μm in diameter, created with a commercial theatrical fog generator) are well mixed with the gas, and the combination is allowed to flow into the test section driven by gravity and mild suction. The volume fraction of the particles in the gas is approximately $1:10^7$. Theoretical and experimental analyses confirming the flow-tracking fidelity of the particles were performed by Rightley *et al.*^{10,11} and Prestridge *et al.*,¹² and included comparisons with direct Rayleigh scattering from the SF_6 without fog present. The geometry of the gas–fog mixture in the test

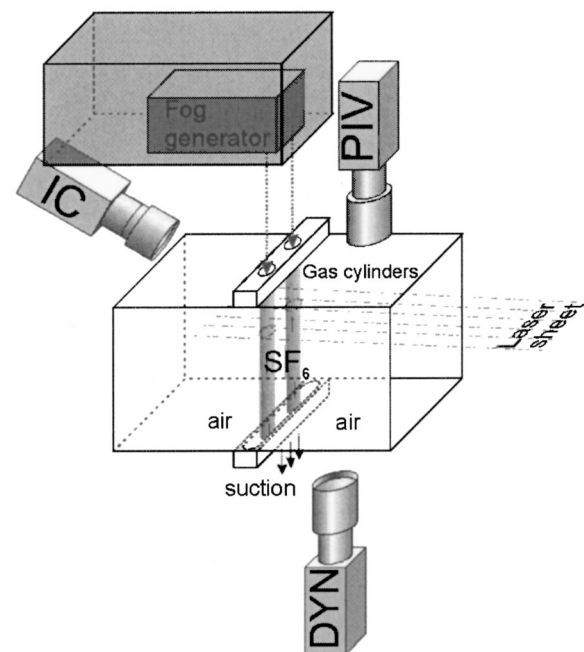


FIG. 2. Schematic of shock tube test section.

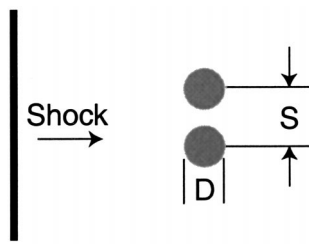


FIG. 3. Schematic of double-cylinder configuration. The initial center-to-center separation, S , is varied from $1.2D$ to $2.0D$, where D is the cylinder diameter.

section depends upon the shape of the output orifice, which in the present experiment is either one nozzle of circular cross-section (to create a single vertical gas cylinder) or two circular nozzles separated spanwise (to create two gas cylinders, as depicted in Fig. 2). The vertical flow velocity (≈ 10 cm/s) is small in comparison with the speed of the shock (≈ 400 m/s) or the convection velocity of the unstable flow structures (≈ 100 m/s). The flow system is modular in that the sections containing the nozzles may be interchanged. Thus, one insert is machined for each geometry, and the initial conditions are changed by simply switching inserts; in this way, the center-to-center spacing, S , of the cylinders is carefully controlled, and adjusted in a repeatable fashion. Each insert is designed to produce a smooth, laminar flow, and visual inspections of the flowing gas reveal steady, two-dimensional cylinders with smooth edges. A more rigorous test of the repeatability and control of the initial conditions (ICs), however, is provided by the actual data. Statistical analysis of the images (presented in a later section) shows high repeatability from shot to shot for each initial spacing on the scales associated with the initial geometry and the primary interfacial instability. Due to the sensitivity of the flow evolution to the initial gas configuration, this repeatability provides strong evidence that the ICs are well-controlled.

A top-view cross-section of the double-cylinder configuration immediately before shock impact is shown schematically in Fig. 3. The cylinders are depicted here with sharp edges, and indeed, images of the initial conditions reveal a relatively sharp interface between the seeded dense gas and the surrounding air. It is likely, however, that as the SF_6 travels downward into the test section, it will diffuse into the air faster than the particles that are embedded within it. Hence, the cylinder edges will not be truly sharp, and the density gradient will be reduced. In the present work, visualization experiments are conducted at *nozzle* separations of $S/D = 1.2, 1.4, 1.5, 1.6, 1.8, \text{ and } 2.0$, where D is the cylinder diameter (here $D \approx 3.1$ mm). These are the spacings referenced in the text; however, due to a slight convergence of the flowing cylinders that occurs immediately below the exit orifice, the actual spacings are slightly different: $S/D \approx 1.09, 1.34, 1.38, 1.54, 1.79, \text{ and } 2.02 (\pm 0.025)$, respectively, as measured from the initial condition images. An additional set of experiments is performed for the case of a single cylinder, for comparison.

B. Visualization

The flow is illuminated with a custom Nd:YAG laser that provides seven pulses (≈ 3 mJ/pulse at 532 nm), each approximately 10 ns in duration, spaced 140 μs apart. The beam is spread to form a horizontal sheet in the test section, parallel with the tube floor (as depicted in Figs. 1 and 2), and is focused down in the vertical direction to less than 1 mm in thickness. Optical access for the beam is provided by a glass window in the tube end section. The timing of the laser (and cameras) relies on a pressure transducer located in the shock tube wall directly upstream of the test section. The laser is timed to provide one pulse immediately before shock impact, to illuminate the initial condition, and six pulses during the postshock flow evolution, before the structures of interest convect out of the test section. All data are acquired before the shock reflected from the end section or the rarefaction from the driver section reach the test section. Approximately 15 realizations are captured at each initial separation. The initial conditions are captured with a Photometrics 512 \times 512 CCD camera, labeled “IC” in Fig. 2, which is tilted at 45° to the light sheet. The image of the initial conditions is remapped to compensate for the combination of the resulting distortion and the “fish-eye” effect produced by the IC lens. The mapping procedure uses bicubic splines. The mapping coefficients are determined by acquiring a distorted image of a test grid, and comparing with the same grid undistorted. The light scattered from the gas during the six postshock (or “dynamic”) laser pulses is captured with a Hadland Photonics 1134 \times 486 gated and intensified camera, labeled “DYN” in Fig. 2, which is aligned normal to the light sheet. This camera does not image individual particles, but collects images of local particle concentration, which in the postshock flow is proportional to the local density (Rightley *et al.*,^{10,11} Prestridge *et al.*¹²). Because the structure is convecting at approximately 100 m/s, the entire event (from the IC capture to the last dynamic pulse) takes less than 1 ms.

C. Particle image velocimetry

In addition to the visualization data, velocity measurements are performed using digital particle image velocimetry (PIV).^{31–33} One velocity field is obtained per realization, and data are acquired at three spacings: $S/D = 1.2, 1.5, \text{ and } 2.0$. In PIV, the flow is seeded with small tracer (fog) particles, though at a concentration less than that typically used for flow visualization, and the particles are illuminated by a pulsed light source formed into a sheet. Typically the sheet is pulsed twice in rapid succession, and the particle images from both pulses are recorded. The displacement of the particles is estimated using a spatial correlation of the intensity, and the velocity vector at a given location is recovered by simply dividing the displacement by the time between the pulses, $\hat{\mathbf{u}} = \Delta \mathbf{X} / \Delta t$.

In the present experiment, the velocity measurements are performed at $t = 750 \mu\text{s}$ after shock passage (corresponding to the sixth dynamic image). The flow cannot at once be

optimally seeded for both PIV and flow visualization; the former requires a uniform distribution of particles throughout the two fluids, and the latter requires a dense distribution of particles within one fluid. Hence, the PIV measurements must be obtained independently from the visualization measurements. Four to seven valid PIV measurements are obtained at each spacing.

The background gas is seeded by injecting particles into the test section prior to release of the shock wave. Any fluctuations introduced by the injection are allowed to die down before the shot is fired. The first of the two required laser pulses is the final pulse from the flow visualization laser; the second is provided by a New Wave Nd:YAG (≈ 10 mJ/pulse at 532 nm) approximately $\Delta t = 3 \mu\text{s}$ after the first pulse. The beams are spread horizontally, to form a sheet, but focused down vertically, so that their focal waists are in the test section. The sheets are carefully aligned to be coplanar within the camera field of view. The scattered light is imaged onto a Kodak Megaplug ES 1.0 8-bit camera, marked “PIV” in Fig. 2, which offers $1\text{k} \times 1\text{k}$ resolution and records the light from the two pulses onto separate frames. The PIV camera focuses only on a small region, $12 \text{ mm} \times 12 \text{ mm}$, through which the unstable structure passes at late time ($t = 750 \mu\text{s}$); the greater magnification permits resolution (and subsequent correlation) of individual particles. The dynamic camera and IC camera are also set to acquire images during each PIV realization. Due to the background seeding, the flow structures in these images are more difficult to visualize, but with slightly higher seeding density in the SF_6 the size and the shape of the structures are visible. These images, in combination with additional flow visualization images (in which only the SF_6 is seeded) obtained immediately before the PIV data, provide confirmation that the structures measured by the PIV are consistent with those measured in the flow visualization.

The PIV images are then interrogated to obtain velocity information. The present interrogation is carried out using a standard two-frame cross-correlation algorithm with discrete window offset (Christensen *et al.*,³⁴ a general description of the algorithm may be found in Raffel *et al.*³⁵). The sizes of the first and second interrogation windows are 32×32 pixels and 64×64 pixels, respectively, and the window overlap is set to 50% to satisfy Nyquist’s sampling criterion (Meinhart *et al.*³⁶). An additional set of interrogations is performed with a first window size of 40×40 pixels for $S/D = 2.0$. These images are slightly noisier than the images at the other spacings, and this window size yields an interrogation quality—in terms of percentage of spurious vectors, as discussed in the following—consistent with the other spacings. This set of velocity fields is used for the $S/D = 2.0$ circulation estimates. The resulting resolution (space between vectors) is $187 \mu\text{m}$ ($234 \mu\text{m}$ for 40×40 interrogation spots). The offset is chosen to place the correlation peak near the center of the correlation plane, and hence remove any bias due to edge effects. A Gaussian three-point estimator is used for correlation peak fitting. Prasad *et al.*³⁷ estimate the random error associated with determination of the correlation peak location as $0.07d_\tau$, where d_τ is the particle image diameter. In the present study, this error is approximately 1.0%–1.5% of the convection velocity. After interrogation, invalid or



FIG. 4. Flow morphologies of a single shock-accelerated gas cylinder at $t = 0, 50, 190, 330, 470, 610,$ and $750 \mu\text{s}$ after shock impact.

spurious vectors are identified by both global and local statistical tests and removed (Westerweel³⁸). The same statistical tests are used to determine if removed vectors may be replaced by the second or third displacement peaks in the correlation plane. This procedure typically removes approximately 3% of vectors; these are then replaced by iterative interpolation. Finally, one pass with a weak Gaussian filter is performed to remove high-frequency noise.

III. FLOW MORPHOLOGIES

Tomkins *et al.*,³⁰ hereafter referred to as “TPRVB,” presented flow morphologies and qualitative analysis of two shock-accelerated, interacting gas cylinders with initial spanwise separation. In this section, we present similar morphologies, and review the relevant points of discussion in TPRVB to place the current quantitative analysis in context.

Before considering the more complex double-cylinder case, let us first review the case of an individual cylinder interacting with a shock wave. Flow morphologies for a single shock-accelerated gas cylinder are presented in Fig. 4. Here, the shock and flow are left to right, and the leftmost image represents the (initial) conditions (ICs) immediately before shock impact. The six subsequent images, from left to right, are acquired at $t = 50, 190, 330, 470, 610,$ and $750 \mu\text{s}$ after shock impact, respectively. Only the SF_6 is seeded, so that image intensity monotonically increases with concentration of SF_6 . The initial condition image has a reduced intensity relative to the six “dynamic” images because it was acquired with a different, nonintensified, camera. Slight variations in image intensity at different “dynamic” exposures are the result of slight variations in laser pulse intensity.

As the shock wave passes through the cylinder, it deposits regions of opposite-sign vorticity on the upper and lower cylinder edges. This vorticity causes nonlinear growth of the interface and rolls up into two vortices, so that the flow is quickly dominated by a counter-rotating vortex pair. At later times, $t = 470 \mu\text{s}$ and beyond, a waviness is present along the air– SF_6 interface; this waviness is interpreted as the manifestation of a secondary instability. The streamwise (W) and spanwise (H_1) dimensions of the single cylinder, as defined by its bounding box, are presented in Fig. 11 along with results for the double-cylinder case. As discussed in TPRVB, however, for purposes of comparison it is sufficient to note that in the single-cylinder case the flow is dominated by two equal strength vortices, and, with the exception of the small scales, the flow morphologies are symmetric about the spanwise midplane.

TPRVB used the insights gained from the single-cylinder experiment to perform a prediction of the flow morphologies in the double-cylinder case. The prediction was based on

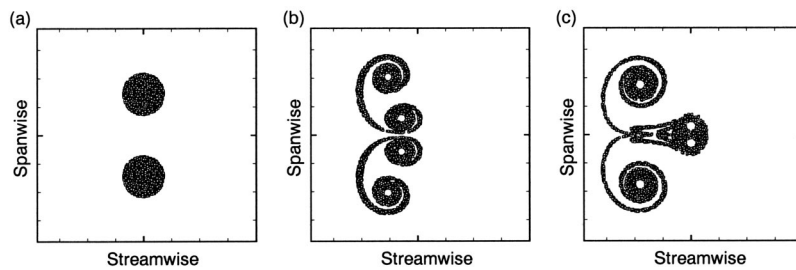


FIG. 5. Vortex blob simulation of two shock-accelerated gas cylinders for $S/D=2.0$. (a) Initial condition; (b) early time; (c) late time.

idealized vortex dynamics implemented in a “vortex blob” simulation (Nakamura *et al.*,³⁹ Rightley *et al.*¹⁰). This incompressible simulation does not capture all of the physics of the flow; rather, it is intended as a rough predictive guide to the flow morphologies given *idealized* vorticity deposition. An initial distribution of vorticity is specified, and the flow is permitted to evolve in time. Flow morphologies are visualized by placing massless “marker particles” in the flow. In the two-dimensional double-cylinder simulation, the marker particles are configured as two circles (or cylinder cross-sections), to represent the dense gas, and the baroclinically deposited vorticity is simulated by placing two “blobs” of equal-strength, opposite-sign vorticity along the upper and lower edges of each cylinder. A vortex “blob” is an ideal point vortex with a correction to create a Gaussian core (instead of a singularity) to reduce numerical errors in the simulation.

The results from the idealized simulation are presented in Fig. 5. The initial spacing is $S/D=2.0$, as seen in Fig. 5(a). The evolution of the cylinders is presented in Figs. 5(b) and 5(c) at early and late time, respectively. At early time, the vorticity deposited around each cylinder rolls up to form an apparent counter-rotating vortex pair, and each vortex entrains the dense gas into its core. These morphologies look qualitatively similar to two single-cylinder morphologies with spanwise separation. One obvious difference is the slight rotation of the structures in the double-cylinder case—an early indication of interaction. At late time, Fig. 5(c), the structures begin to deviate more significantly from the single-cylinder case. The two inner vortices, also counter-rotating, are mutually induced downstream relative to the outer vortices. Hence, the vortex blob simulations suggest that even at the largest separation, interaction between the cylinders may significantly affect the resulting flow structures. The results from these idealized simulations are supported by two recent computational efforts,^{40,41} which yield flow morphologies that are qualitatively consistent with the vortex blob results at $S/D=2.0$.

Flow morphologies for the double-cylinder case are presented in Figs. 6–8. As in Fig. 4, each image contains an initial condition and six postshock or dynamic exposures. Measurements are performed at six values of the center-to-center spacing: $S/D=1.2, 1.4, 1.5, 1.6, 1.8,$ and 2.0 , nominally. The high repeatability of the data permits presentation of only one realization per spacing—each image is representative of the ensemble of data (at a given spacing). TPRVB classified the data sets into three groups, depending on the degree of interaction associated with each spacing; the

groups were labeled “strong,” “moderate,” and “weak” interaction. Two spacings are associated with each category.

Examples of “weak interaction” are presented in Fig. 6. The initial cylinder separations are $S/D=2.0$ and 1.8 . Following TPRVB, in weak interaction cases the resulting flow structures look qualitatively similar to two single-cylinder morphologies, and two vortices form per cylinder. The interaction between the cylinders creates slow rotation and an alteration of the trajectory of the structures.

The morphologies presented in Fig. 6(a) for $S/D=2.0$ are clearly different from those predicted by the (idealized) vortex blob simulation at the same initial spacing. While in both sets of results the deposited vorticity rolls up into two counter-rotating vortex pairs, the rotation of the structures induced by the vortices is different—in the computations, the innermost vortices are induced downstream, while in the experiment, the innermost vortices move upstream, relative to the outer vortices, and outwards. TPRVB offer the following interpretation of this difference. The simulated results are consistent with the motion of idealized vortices, of equal strength, in a plane. The experimental results, then, are at odds with the motion of idealized vortices of equal strength—but would be consistent with idealized vortex dynamics if the outer vortices were stronger than the inner ones. In Sec. V, we present vorticity measurements that support this hypothesis and quantify the relative vortex strengths.

Examples of flow morphologies resulting from “moderate interaction” are presented in Fig. 7. Here, the initial separations are $S/D=1.6$ [Fig. 7(a)] and $S/D=1.5$ [Fig. 7(b)].

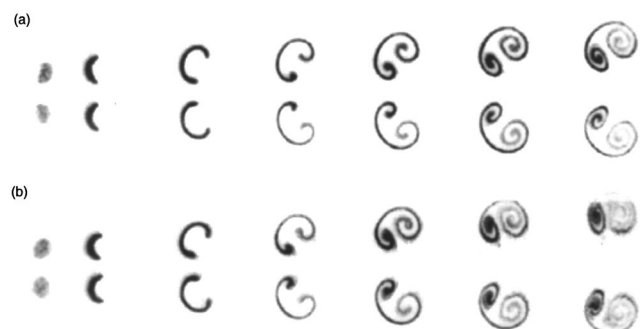


FIG. 6. Flow morphologies for two interacting, shock-accelerated gas cylinders: weak interaction. Images at $t=0, 50, 190, 330, 470, 610,$ and $750 \mu\text{s}$ after shock impact. (a) $S/D=2.0$; (b) $S/D=1.8$.

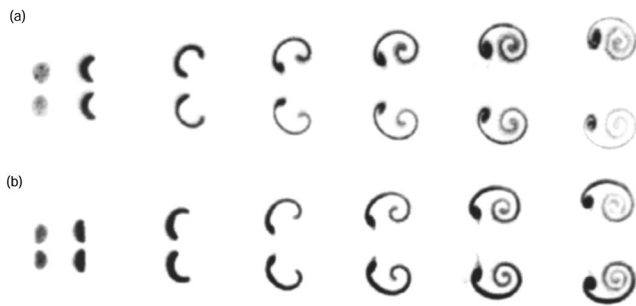


FIG. 7. Flow morphologies for two interacting, shock-accelerated gas cylinders: moderate interaction. Images at $t=0, 50, 190, 330, 470, 610,$ and $750 \mu\text{s}$ after shock impact. (a) $S/D=1.6$; (b) $S/D=1.5$.

TPRVB attach the label “moderate” to these spacings because in the resulting morphologies two vortices continue to form per cylinder, but now the formation of the inner vortices is severely retarded—they simply appear as rolled-up disks (or columns, in three dimensions) of dense gas. Hence, the actual flow structures are being altered, in addition to the rate of rotation.

In Fig. 8, flow morphologies for the case of “strong interaction” are shown, with nominal initial spacings of $S/D=1.4$ and 1.2 . In these cases, the flow structures are fundamentally altered; specifically, the inner vortices do not appear to form at all, and the flow is completely dominated by the outer vortices. The smallest initial separation [Fig. 8(b)] produces a structure that is both qualitatively and quantitatively very similar to the single-cylinder case (see measures W and H_1 in Fig. 11, which are within 7% and 3% for the two cases, respectively). Note also the existence of waviness along the air-SF₆ interface, evidence of a secondary instability, as seen in the single-cylinder visualizations.

Previous data for comparison with the observed morphologies are scarce. To the authors’ knowledge, only one previous study has considered the double-cylinder problem. Yang *et al.*⁵ performed a computational study in which they focused on shock-accelerated, light-gas single cylinders, but several other cases were simulated as well, including double-cylinder configurations with spanwise spacings of $S/D=1.2, 1.5, 2.0,$ and 3.0 impacted by a Mach 1.1 shock. The authors investigated shock-induced mixing using the stretching rate of the material interface as the relevant metric, and found a higher rate for the two smaller spacings relative to the larger ones. A similar analysis on the present data does not reveal a clear trend like that seen in the numerical study, however. This is perhaps due to the obvious differences in the two studies and/or the high level of small-scale activity observed in the experimental results that is not typically present in computations (which may strongly affect the interface length, particularly at late time).

The TPRVB visualization results clearly reveal that the degree of interaction, and hence the resulting flow morphology, is highly sensitive to the initial cylinder separation. An excellent example of this sensitivity, as discussed in TPRVB, is the possible existence of a bifurcation point in the flow as S/D decreases below 1.5. The branches of this apparent bifurcation would correspond to the postshock formation of

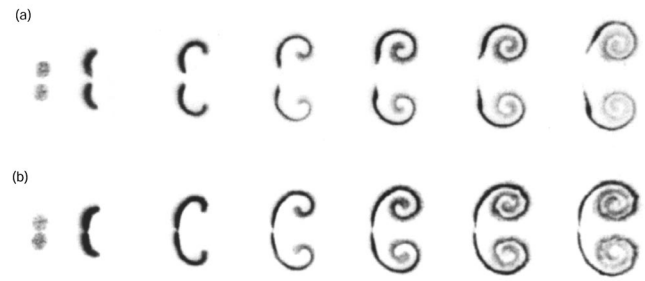


FIG. 8. Flow morphologies for two interacting, shock-accelerated gas cylinders: strong interaction. Images at $t=0, 50, 190, 330, 470, 610,$ and $750 \mu\text{s}$ after shock impact. (a) $S/D=1.4$; (b) $S/D=1.2$.

two and four vortices. Hence, an alteration of the initial spacing by a mere 7% ($S/D=1.4$ to 1.5) appears to lead to very different flow morphologies. TPRVB proposed two mechanisms by which this keenly sensitive interaction may occur. One possibility is the mutual annihilation, or attenuation, of the inner vortices a short time after shock passage. The resulting inner vortices would then be weaker than the outer ones, and decreased spacing would lead to increased attenuation. A second possibility is that the presence of a second cylinder in close proximity to the first affects the shock propagation through the cylinders, and thus alters the initial baroclinic vorticity deposition, particularly on the inner cylinder edges. In the following sections, we present analysis quantifying the effects of this interaction and providing insight into the underlying mechanisms involved.

IV. LARGE-SCALE DYNAMICS OF CONCENTRATION FIELDS

In this section, we present quantitative analysis of the flow visualization images with the goal of characterizing the large-scale dynamics of the concentration fields. Several measures are introduced, using analogy to solid mechanics concepts, to quantify the geometry of the structures in terms of position and rotation. A new rotationally invariant measure of the mixing width is also described.

Several relevant scales are distinguishable in the vortex dynamics of the shock-accelerated gas-cylinder pair (as shown in Fig. 9). The largest is the scale of the pair of deforming gas cylinders (scale 1). Let us denote the scale of a single deforming cylinder (or “mushroom cap”) as scale 2, followed by the scale of a single vortex forming due to the initial baroclinic instability (scale 3). Finally, the smallest scale is that of the vortices and interfacial undulations associated with the secondary instability (scale 4).

While an understanding of the vortex dynamics on the two smallest scales (3 and 4) requires knowledge of the velocity field, a lot about the behavior of the larger features can be inferred from flow visualization (see, e.g., Fig. 7). In previous studies dealing with either a shock-accelerated gas curtain (Rightley *et al.*,^{10,11} Prestridge *et al.*¹³) or a single gas cylinder (Prestridge *et al.*²²), the quantifiable “integral scale” usually employed for benchmarking was the mixing

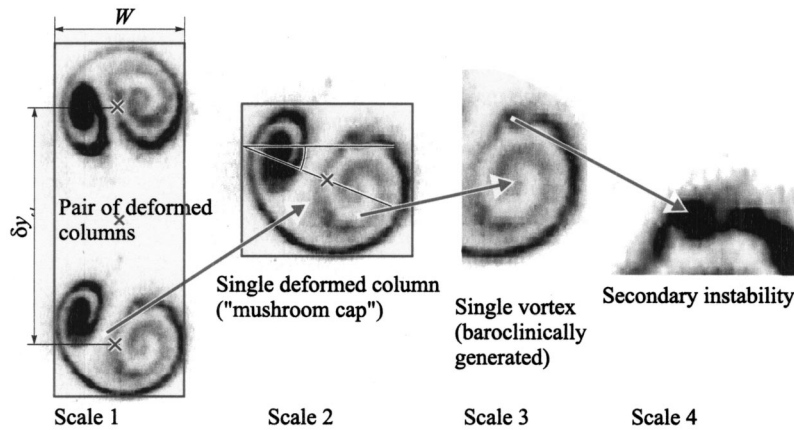


FIG. 9. Schematic of the relevant scales in the vortex dynamics of the system.

zone width, i.e., the streamwise extent of the flow structure forming due to the RM instability. Both in the case of the gas curtain and the single cylinder, the vortices formed by the initial shock interaction experience little relative movement; this is untrue, however, for the interacting gas-cylinder pair. To appropriately evaluate the mixing zone width in this case, we must take into account not just the expansion of the “mushroom caps” (scale 2) due to vortex roll-up, but their rotation as well.

We introduce several measures for flow visualization images, which are interpreted as concentration maps of the heavy gas. Examples of these measures are depicted in Fig. 10, which shows a dynamic image sequence of an evolving gas cylinder pair at $S/D=1.6$ for scale 1 (top) and scale 2 (bottom). These measures find analogy with notions from solid mechanics. For a system of N particles with masses m_k with coordinates (x_k, y_k) , $k=1 \dots N$, the coordinates of the center of mass are

$$x_{cm} = \frac{\sum_{k=1}^N m_k x_k}{\sum_{k=1}^N m_k}, \quad y_{cm} = \frac{\sum_{k=1}^N m_k y_k}{\sum_{k=1}^N m_k}. \quad (1)$$

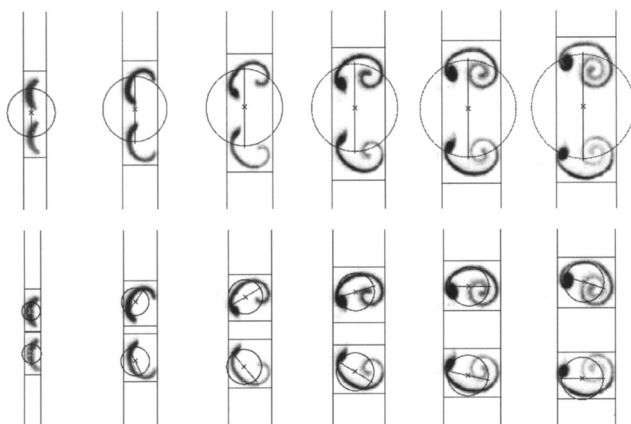


FIG. 10. Integral scales characterizing scales 1 (top) and 2 (bottom) of an evolving gas-cylinder pair with $S/D=1.6$. Vertical lines denote the mixing-zone width for each exposure, and horizontal lines are added to show the bounding boxes for each scale. Centers of intensity (x_{cl}, y_{cl}) are marked in each dynamic exposure (\times). Circles show radii of intensity r_I [Eq. (3)], and lines crossing the circles correspond to the main axis of intensity (see description in text).

An exposure in the flow-visualization bitmap can be interpreted as a sequence of intensity values I_{ij} , where (i, j) are the pixel coordinates corresponding to the physical space position $(i\Delta x, j\Delta x)$, Δx being the pixel resolution (which is the same in the x and y directions). As discussed in Sec. II, previous research has shown that the intensity I_{ij} of light scattered by the fog droplets in the plane of the laser sheet grows monotonically with SF_6 concentration. We can subtract the background intensity level associated with unseeded air and then, using analogy with Eq. (1), define the center of intensity (x_{cl}, y_{cl}) of each exposure thus:

$$x_{cl} = \Delta x \frac{\sum_{i,j} I_{ij} i}{\sum_{i,j} I_{ij}}, \quad y_{cl} = \Delta x \frac{\sum_{i,j} I_{ij} j}{\sum_{i,j} I_{ij}}, \quad (2)$$

where the summation boundaries in i and j define a rectangular region containing the exposure (as seen in the top half of Fig. 10). Moreover, for two-cylinder experiments, one can define the center of intensity for each cylinder (or mushroom cap, as seen in the bottom half of Fig. 10). A nonlinear relationship between I_{ij} and the average SF_6 concentration in the area corresponding to the pixel might lead to errors in the estimate of (x_{cl}, y_{cl}) . As will be seen, however, the overall behavior of the intensity-based measures reveals that no systematic errors arise due to this imperfection.

To provide a quantitative measure of gas-cylinder evolution similar to the mixing-zone width in earlier work but rotationally invariant, we introduce the radius of intensity for a deforming gas cylinder:

$$r_I^2 = \frac{\sum_{i,j} I_{ij} ((x_{ij} - x_{cl})^2 + (y_{ij} - y_{cl})^2)}{\sum_{i,j} I_{ij}}, \quad (3)$$

where (x_{cl}, y_{cl}) are the coordinates of the center of intensity of the mushroom cap and the i, j summation takes place in a rectangular area enclosing the cap (Fig. 9, scale 2). The solid mechanics analog of r_I is the radius of inertia. Examples of radii of intensity for $S/D=1.6$ are depicted as superimposed circles in Fig. 10 for scales 1 (top) and 2 (bottom).

A comparison of the “old” integral measure (streamwise mixing-zone width, W) and the “new” one (radius of intensity for scale 2, hereafter referred to as r_2) is presented in

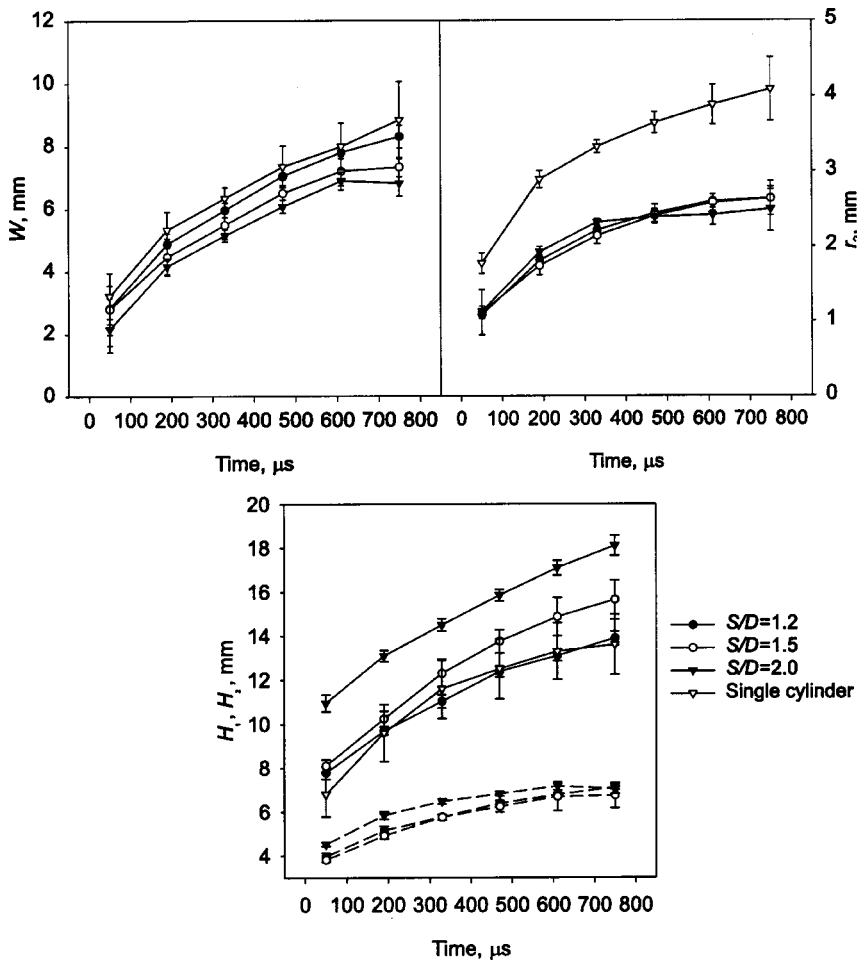


FIG. 11. Evolution of the mixing-zone width, W (top left), the radius of intensity [Eq. (3)] for scale 2, r_2 (top right), and the heights H_1 (dashed lines) and H_2 (solid lines) for scales 1 and 2, respectively (bottom). Curves corresponding to different initial conditions are labeled in the plot.

Fig. 11. In this and all following comparisons in this section, quantities are averaged over all realizations. The mixing-zone width exhibits nonmonotonic growth for the initial spacing $S/D=2.0$ due to the rotation of the “mushroom caps”—a physically unrealistic behavior. Note also that the overall mixing-zone width appears to be the largest for the control case of the single cylinder and decreases as S/D increases.

The radius of intensity of scale 2 (“mushroom caps”) clearly shows the influence of cylinder interaction, decreas-

ing dramatically (by a factor of about 1.5) from the single-cylinder case to the double-cylinder cases. The dependence of r_2 upon the initial cylinder separation is weaker, although there is some evidence that “weak” cylinder interaction is characterized by faster initial growth of r_2 . This is consistent with the much faster growth of r_2 in the control case (single cylinder). Note that r_2 does grow monotonically with time, and is thus considered a more appropriate integral scale for the present problem. For thoroughness we also include the integral measures associated with the total height (spanwise

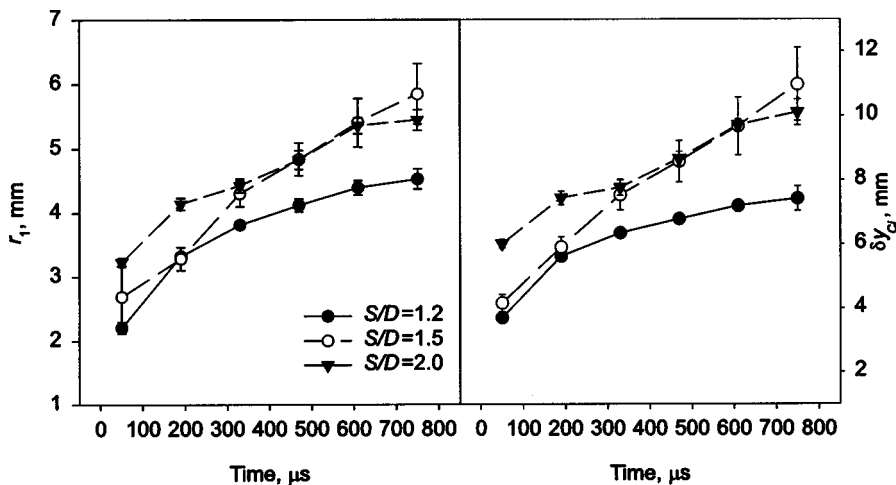


FIG. 12. Evolution of the radius of intensity [Eq. (3)] for scale 1, r_1 (left), and cross-flow distance between the centers of intensity, δy_{c1} (right). Curves corresponding to different initial conditions are labeled in the plot.

dimension) of the structures (H_1) and the height of the individual mushroom caps (H_2).

The behavior of the radius of intensity of scale 1, r_1 , appears to be dominated by the distance between the “mushroom caps” (see Fig. 12). To confirm this, we also plot the cross-flow spacing of the “mushroom cap” centers of intensity δy_{c1} in Fig. 12. Strictly speaking, for $S/D=1.2$ one cannot speak of the deforming cylinders as “mushroom caps” because they do not form vortex pairs; however, our analysis method does not make explicit use of the flow morphology. The trends in r_1 and δy_{c1} are very similar: the fastest cross-flow growth is present in the $S/D=1.5$ case, and it is slower for the cases with greater initial separation between the cylinders.

The mixing-zone width W is influenced by the rotation of the “mushroom caps.” The new integral measures r_1 and r_2 are deliberately selected to be rotationally invariant. How do we characterize the rotation on scale 2? Principles of solid mechanics can be exploited further by introducing the moment of intensity about an axis, similar to the moment of inertia. For an axis passing through (x_{c1}, y_{c1}) at an angle α with the streamwise coordinate axis (measured counterclockwise), the expression

$$I(\alpha) = \frac{\sum_{i,j} I_{ij} ((x_{ij} - x_{c1}) \sin \alpha - (y_{ij} - y_{c1}) \cos \alpha)^2}{\sum_{i,j} I_{ij}}, \quad (4)$$

describes the central moment of intensity about the axis. The value of α corresponding to the maximum of $I(\alpha)$ denotes the direction of the *main axis of intensity* (analogous to the main axis of inertia, and represented by a straight line through the center of intensity in Fig. 10). Figure 10 shows that the main axis of intensity of scale 1 is oriented spanwise, as expected by symmetry, and that the main axis of intensity of a mushroom cap aligns quite well with its orientation. Thus, the change in the direction of this latter axis serves as a reliable indicator of the rotation on scale 2. Rotation angle as a function of time and the average rotation rate for the “mushroom caps” forming at $S/D=1.5$ and greater are presented in Fig. 13. The rotation angle (seen in the left-hand plot) is constant with respect to spacing for the first and second dynamic exposures, but differences between the spacings become obvious at the third exposure and later in time.

As seen qualitatively in the visualizations, the rotation angle increases with decreasing S/D . The rate of rotation is shown on the right-hand side of Fig. 13. The “moderate” interaction cases are observed to rotate more quickly, with the case of $S/D=1.5$ characterized by the fastest rotation rate (about 2500 s^{-1}). As the initial cylinder spacing increases to $S/D=2.0$, this rate drops to 1200 s^{-1} . Following the hypothesis of TPRVB, this relationship between the rotation rate and S/D may be interpreted as a manifestation of a strength disparity between the inner and outer vortices at each spacing. We confirm this theory in Sec. V using velocity-field measurements.

V. MEASUREMENT AND ANALYSIS OF VELOCITY AND VORTICITY FIELDS

In Sec. IV, we quantitatively examine the large-scale concentration fields and how these fields evolve over time. The principal mechanism behind this evolution is vorticity induction. In the present section, we quantify the vorticity fields that drive this induction.

We present two-dimensional, planar velocity (PIV) measurements at late time ($t=750 \mu\text{s}$) for three spacings: $S/D=2.0, 1.5$, and 1.2 . Out-of-plane vorticity calculations based on these measurements are then presented, including the absolute and relative strengths (circulations) of the vortices. Additional vortex blob simulations are also performed based on these experimental estimates of relative vortex strength. The details of the PIV image acquisition and analysis are provided in Sec. II. As discussed in Sec. II, the velocity measurements are performed independently of the flow visualization, and the difficulty of the measurements complicates acquisition of a statistically significant number of realizations (four to seven are captured at each spacing). It is nonetheless possible to draw conclusions based on these realizations because of the high repeatability of the experiment.

A. Velocity fields

A sample PIV image is shown in Fig. 14 for $S/D=2.0$. The image is one of two taken for each realization (the other looks very similar), and it is oriented to match the visualization data (i.e., the flow is left to right). The camera field of

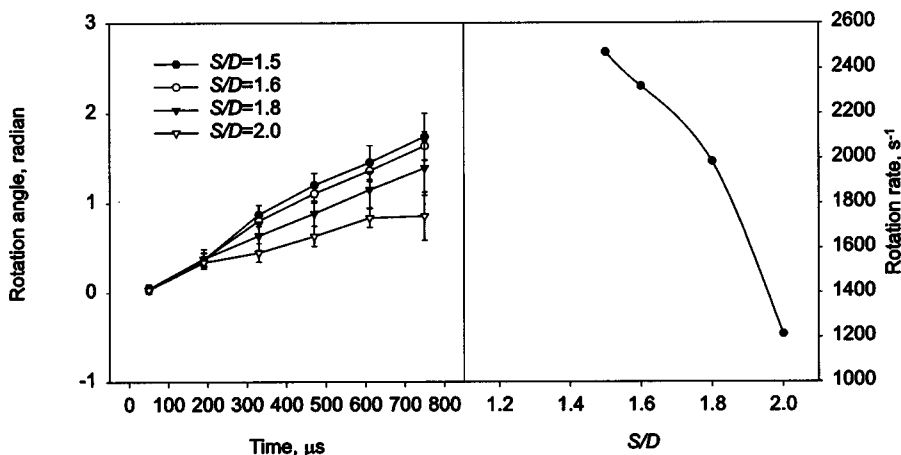


FIG. 13. Rotation angle of “mushroom caps” vs time after shock passage (left), and the average rotation rate as a function of the initial cylinder spacing, S/D (right).

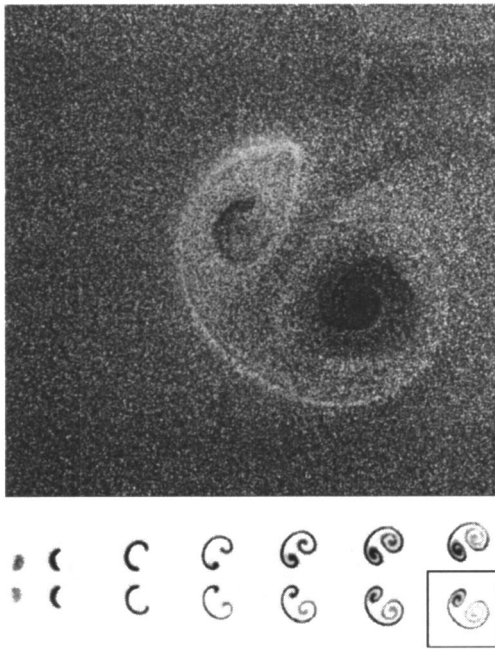


FIG. 14. Sample PIV image at $t \approx 750 \mu\text{s}$ for $S/D=2.0$. The image is the second of two images acquired per realization. PIV field of view is represented by box in the reference image below.

view extends slightly across the spanwise midplane of the double-cylinder structure, so that one of the two unstable cylinders is captured on each shot. The captured area is depicted in a reference visualization image below the PIV image in Fig. 14—the box represents the camera field of view. The timing of the measurement corresponds to the sixth dynamic flow visualization exposure. The timing and field of view are fixed for all shots and spacings.

PIV velocity vector maps are presented in Fig. 15 for $S/D=2.0$, 1.5, and 1.2. One sample realization is selected per spacing; however, as with the visualization results, the selected realizations are representative of the body of data (for a given spacing). In each plot, a streamwise convection velocity, $U_c \approx 100 \text{ m/s}$, is subtracted from the total field, and the plotted velocity vectors are fluctuating relative to this frame, so that the viewer is effectively moving in a frame with the structure. This permits proper visualization of the vortices (Adrian *et al.*⁴²). A reference vector of 15 m/s is also included on each plot. This magnitude approximately corresponds to the rms fluctuating velocity magnitude, and is also approximately one-half of the maximum fluctuating velocity magnitude on each plot. Adjacent to each velocity field is one of the two PIV images from which the velocity is calculated. As discussed earlier, optimum PIV seeding is completely uniform, but slight differences in seeding density between the SF_6 and air permit crude visualization of the flow structures while maintaining a sufficiently high PIV signal-to-noise ratio for reliable measurements. This crude visualization is sufficient to provide a structural reference for the velocity data. The approximate locations of the vortex cores are represented by white dots.

Velocity vectors for $S/D=2.0$ are seen in Fig. 15(a). As expected, the flow is dominated by two counter-rotating vor-

tices, which correspond to the two regions of roll-up in the associated raw PIV image. As in the single-cylinder case, the region between the vortices is subject to the greatest induction, with peak fluctuating velocities around 30 m/s. The outer (lower in this view) vortex qualitatively appears larger and stronger, and the angle between the two is consistent with the earlier visualization results (and, of course, the associated PIV image).

A velocity field for a moderate interaction case, $S/D=1.5$, is presented in Fig. 15(b). The outer vortex is again obvious and appears to be the dominant structure of the flow. More careful inspection of the plot also reveals a small, apparently weaker, inner vortex, located at approximately $x=2.5 \text{ mm}$, $y=4.5 \text{ mm}$. The core of this vortex is moving with a spanwise velocity of $V_c=6 \text{ m/s}$ with respect to the reference frame moving with the streamwise convection velocity ($U_c=100 \text{ m/s}$). This velocity is induced by the dominant outer vortex, which sweeps the weaker vortex outward. The appearance of velocity vectors corresponding to circular streamlines in a given reference frame provides strong evidence that (i) a vortex exists at this location, and (ii) this vortex is moving at the subtracted convection velocity.⁴² Thus, the “disk” of dense gas visualized in Fig. 7(b) at late time actually corresponds to a small vortex, and is likely being rotated around the dominant (outer) vortex, as hypothesized earlier.

Figure 15(c) presents a velocity field for an initial spacing of $S/D=1.2$. As suggested by the visualization data, the late-time flow is dominated by a single vortex from each cylinder; the two cylinders thus form a counter-rotating vortex pair. As in the single-cylinder case, the greatest induced velocities lie on the spanwise midplane.²² These velocity maps also contain information about the smaller flow scales, although this information is not readily apparent in the plot because of the strength of the two dominant vortices (larger scales). Small-scale fluctuations are typically manifest as discontinuities between vector lengths or directions; careful examination of Figs. 15(a)–15(c) will reveal such discontinuities. Small-scale activity is more readily revealed, however, in vorticity maps.

B. Vorticity fields

The out-of-plane vorticity, ω_z , is calculated from the two-dimensional velocity field as follows. At a given point, one defines a 3×3 neighborhood of vectors around the point in question and calculates the local circulation about this point by line integrating the scalar product of the velocity vectors and the differential vector length over the eight surrounding vectors (Stokes’ theorem is used to relate the line integral to the circulation). The vorticity is obtained by dividing by the area within the contour defining the neighborhood (Reuss *et al.*⁴³):

$$\omega_z = \frac{1}{A} \oint_C \mathbf{u} \cdot d\mathbf{l}. \quad (5)$$

Instantaneous vorticity maps for the three realizations in Fig. 15 are presented in Fig. 16. For $S/D=2.0$, seen in Fig. 16(a), the results are consistent with expectation: two large

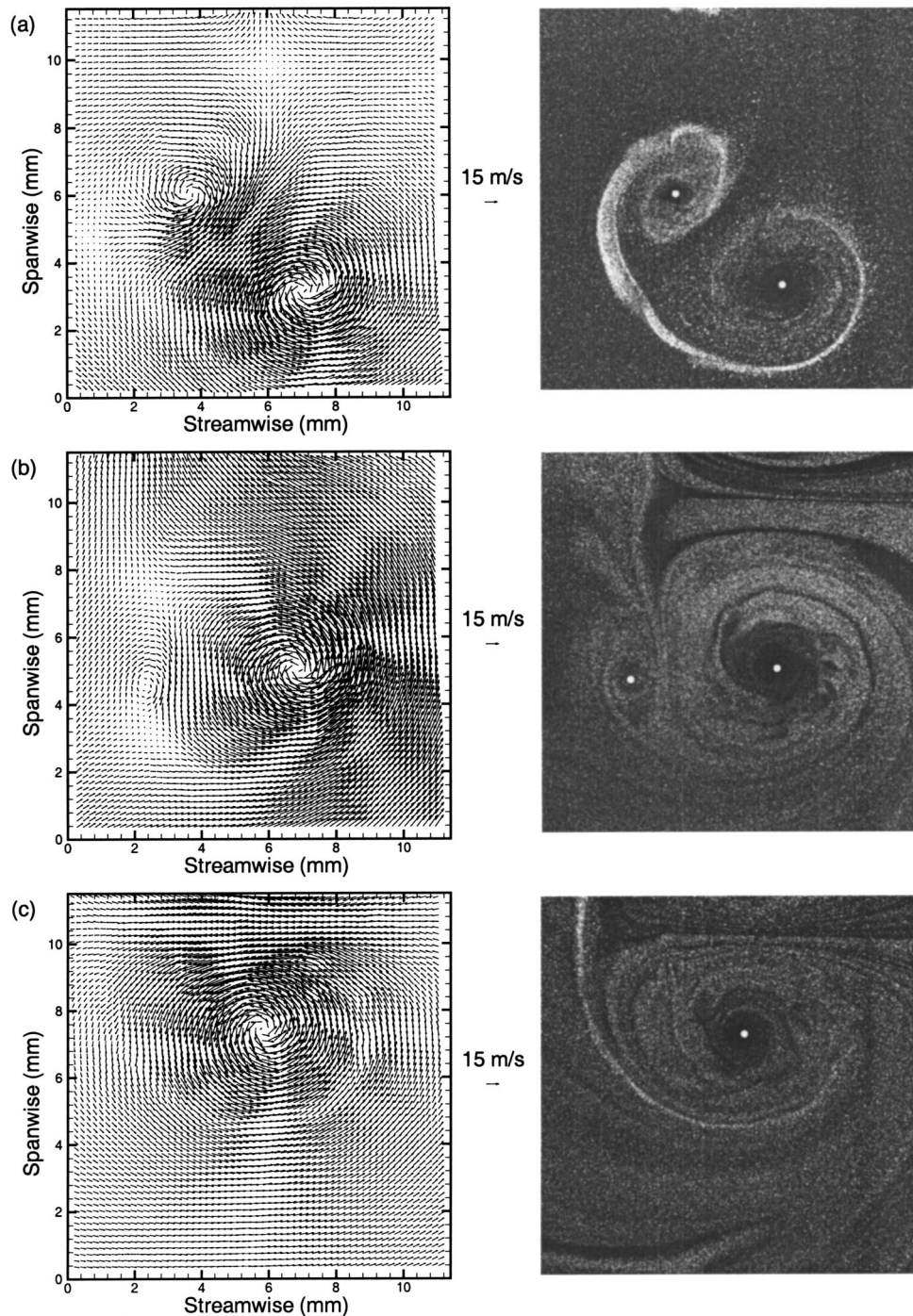


FIG. 15. Instantaneous velocity fields for one of two shock-accelerated gas cylinders at $t = 750 \mu\text{s}$. Vectors are fluctuating relative to the frame in which the structure is convecting ($\approx 100 \text{ m/s}$, left to right). Field of view as in Fig. 14. One PIV image associated with each velocity field is also included for reference, with the approximate location of vortex cores represented by white dots: (a) Weak interaction, $S/D = 2.0$; (b) moderate interaction, $S/D = 1.5$; (c) strong interaction, $S/D = 1.2$.

regions of opposite-sign vorticity exist at the apparent locations of the vortices in the velocity field. The outer vortex (positive vorticity) is larger than the inner one, but the inner structure still has relatively high levels of vorticity ($|\omega_z| > 50 \text{ 1/ms}$) within its core.

Inspection of vorticity maps at the other spacings, $S/D = 1.5$ [Fig. 16(b)] and $S/D = 1.2$ [Fig. 16(c)], reveals simi-

larities between the three. In particular, the vorticity pattern associated with the outer vortices is strikingly similar in each case. The core consists of a region of intense vorticity, with levels of ω_z decreasing with increasing radial distance from the core. Also, the strength of these vortices appears to remain roughly constant with spacing, qualitatively—despite the fact that the basic morphologies exhibit a keen sensitivity

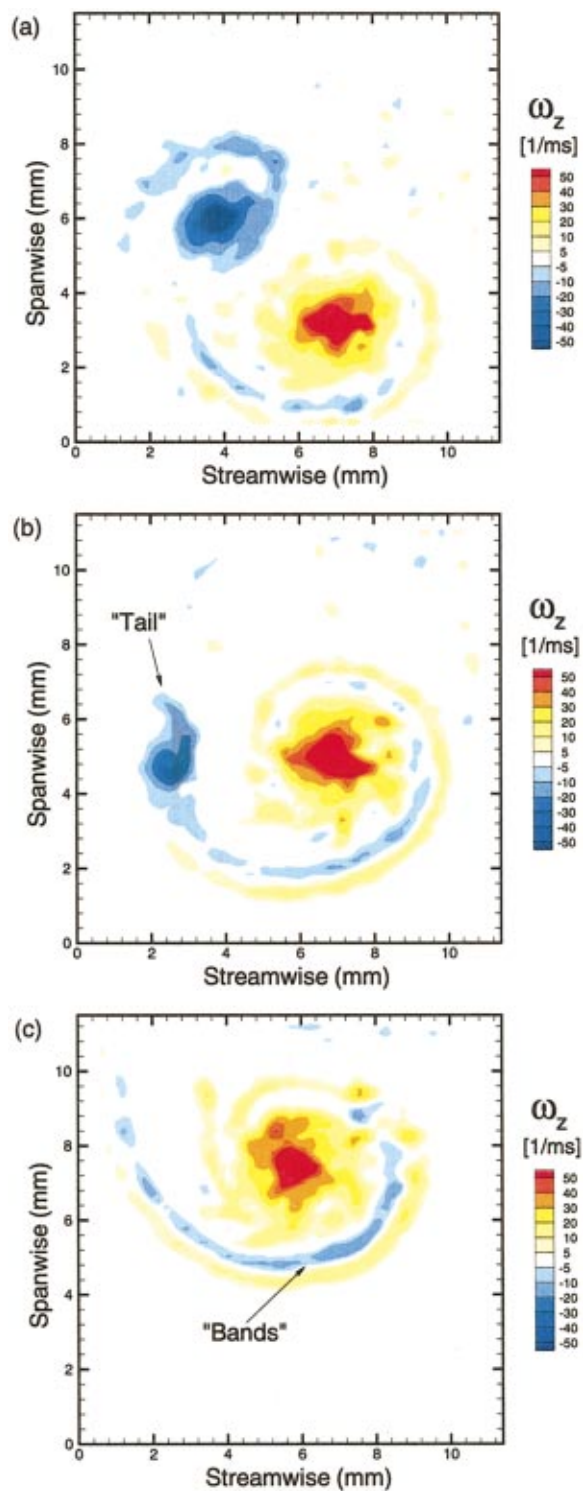


FIG. 16. (Color) Instantaneous vorticity fields for one of two shock-accelerated gas cylinders. Results are calculated from the velocity fields in Fig. 15. Field of view as in Fig. 14. (a) Weak interaction, $S/D=2.0$; (b) moderate interaction, $S/D=1.5$; (c) strong interaction, $S/D=1.2$.

to spacing. Long bands of positive and negative vorticity are observed to curl outwards from the outer vortex core in each case toward the inner vortex (or toward the spanwise mid-plane, in the case of $S/D=1.2$). These bands of vorticity are associated with the bands of dense gas seen in the flow visualization, which connect the outer and inner structures. The

vorticity bands are interpreted as regions of shear along the air-SF₆ interface, created by velocity differences between the SF₆ and air, although baroclinic mechanisms may also be active (Cook and Miller,²³ Zabusky²⁴). In some cases, smaller-scale structure is apparent in these bands. For example, a waviness of the vorticity contours is evident in Fig. 16(a), which is likely associated with the waviness of the air-SF₆ interface observed in the visualization (recall that this is interpreted as a manifestation of a secondary instability). A thorough investigation of this small-scale structure is beyond the scope of the present paper.

In contrast with the outer structures, the characteristics of the inner vortices change significantly with spacing. The inner vortex in Fig. 16(a) ($S/D=2.0$) appears relatively strong. Indeed, visualizations show that the inner vortex induces significant roll-up of the dense gas associated with a band of vorticity, similar to that seen in the stronger outer vortices. As the structures move closer together, as in Fig. 16(b), the inner vortex now appears significantly weaker, consistent with the interpretation of TPRVB. The area of the structure and its peak levels of vorticity are significantly reduced. It is interesting to note that a small “tail” of negative vorticity [located at approximately $x=2.4$ mm, $y=6.4$ mm in Fig. 16(b)] appears to form from the inner vortex. This feature, although subtle, is not unique to this realization—it also appears in the other vorticity maps at this spacing. Moreover, the visualizations reveal a similar “tail” of dense gas emerging from the “disks” of gas associated with the inner vortices at this spacing [see results at $t=610$ and 750 μ s in Fig. 7(b)]. Inspection of Fig. 7(b) reveals that this concentration tail first becomes apparent at the second dynamic exposure, $t=190$ μ s, and grows until it is most obvious at $t=610$ μ s. At $t=750$ μ s, however, it is far less obvious than at the previous exposure. This apparent disappearance of SF₆ is rather mysterious, until one considers the vorticity distribution evident in Fig. 16(b). The tail of vorticity, and the vorticity associated with the vortex itself, would likely act to entrain the concentration tail back toward the vortex core. Hence, this “disappearance” of the dense gas might well be real, and a simple consequence of vortex induction. Unfortunately, with the present data, the mechanisms behind the initial formation of the concentration tail, and its subsequent growth, are unclear.

Finally, for the case of “strong” interaction, seen in Fig. 16(c), the vorticity maps reveal no concentration of vorticity that might correspond to an inner vortex. This observation, of course, is consistent with our interpretation of the flow visualization results, but now we have quantitative confirmation that no inner vortex exists at late time for $S/D=1.2$. Thus, it appears from Fig. 16 that the outer vortices do not change significantly with initial cylinder spacing, but that the inner vortices become significantly weaker with decreasing spacing, and, in the limiting case of strong interaction, cease to exist.

We may rigorously investigate these interpretations by explicitly calculating the circulation for the inner and outer vortices. In Fig. 17, the vortex circulation Γ is plotted as a function of initial cylinder spacing for both inner and outer vortices in all realizations. The strength of the outer vortices,

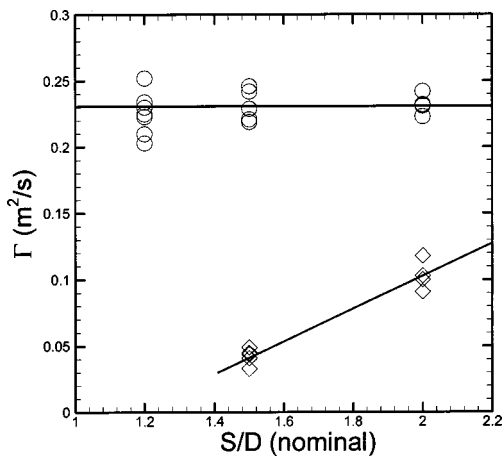


FIG. 17. Circulation, Γ , vs nominal initial spacing, S/D , for both inner and outer vortices in all realizations: (○) outer vortices; (◇) inner vortices.

represented by circles, is roughly constant for all spacings considered. In fact, the mean values of outer-vortex circulation for the cases of $S/D=1.2, 1.5,$ and 2.0 are $\Gamma_o=0.225, 0.231,$ and 0.232 m^2/s , respectively, where the subscript “ o ” denotes the outer vortex. Thus, the strength of the outer vortices appears to be independent of the initial cylinder spacing, and hence, the degree of interaction.

The circulations of inner vortices, represented by diamonds, are also plotted for $S/D=2.0$ and 1.5 . At $S/D=2.0$, it turns out that the inner vortices are substantially weaker than the outer ones, even though the flow visualization images reveal that they induce substantial roll-up of the dense gas. Their mean circulation is $\Gamma_i=0.103$ m^2/s (where the subscript “ i ” denotes inner). The resulting ratio between the outer and inner vortices is $\Gamma_{oi}=\Gamma_o/\Gamma_i=2.25$. Thus, even the greatest spacing ($S/D=2.0$) shows a significant degree of interaction. At $S/D=1.5$, the mean circulation is $\Gamma_i=0.042$ m^2/s , much lower than Γ_o . In this case, $\Gamma_{oi}=5.5$. It should be noted that in all cases, the data show relatively little scatter, particularly when considered in the context of shock-accelerated, RM-unstable flows. This consistency is a

testament to the repeatability of the experiment itself, and it also provides indirect, but important, validation of the diagnostic.

These quantitative results confirm the interpretation of the flow visualization data offered by TPRVB, i.e., that the inner vortices are weakened by interaction, and that the stronger outer vortices induce the inner ones upstream and eventually outwards at late time. The data also show a less anticipated result, that the strength of the outer vortices is not affected by the initial cylinder spacing, and they allow us to attach approximate quantitative measures to our degree of interaction labels: strong, $\Gamma_{oi}\approx\infty$; moderate, $4<\Gamma_{oi}<10$; and weak, $\Gamma_{oi}<4$.

In addition to the above-discussed data, a second set of velocity/vorticity measurements is performed for the case of $S/D=2.0$. These results suffer, however, from an experimental error: a failure to monitor the concentration of the SF_6 in the seeding box, from which the gas cylinders are formed. As a result, the cylinders were not pure SF_6 , but an air- SF_6 mix of unknown concentration. The resulting data clearly exhibit characteristics of reduced baroclinic vorticity production: low roll-up of dense gas around the vortex cores (from visual inspection) and weak inner and outer vortices (from PIV-based circulation estimates). The results, however, permit examination of the effects of SF_6 concentration on vorticity production. Consider the plots shown in Fig. 18. In Fig. 18(a), the circulation ratio, Γ_{oi} , is plotted against S/D . Included are the data in Fig. 17, at $S/D=1.5$ and 2.0 (represented by circles), and the additional low- SF_6 results at $S/D=2.0$ (seven realizations, represented by diamonds). The data collapse extremely well for $S/D=2.0$ —a total of 11 data points are plotted in that cluster—even though the concentration of SF_6 in the cylinders is varying. Thus, in the two-cylinder problem, the outer:inner vortex circulation ratio appears to be roughly constant with respect to Atwood number, $A=(\rho_1-\rho_2)/(\rho_1+\rho_2)$ for $S/D=2.0$, over the range of A studied.

An estimate of the variation in SF_6 concentration, and hence the range of A measured, may be inferred from Fig.

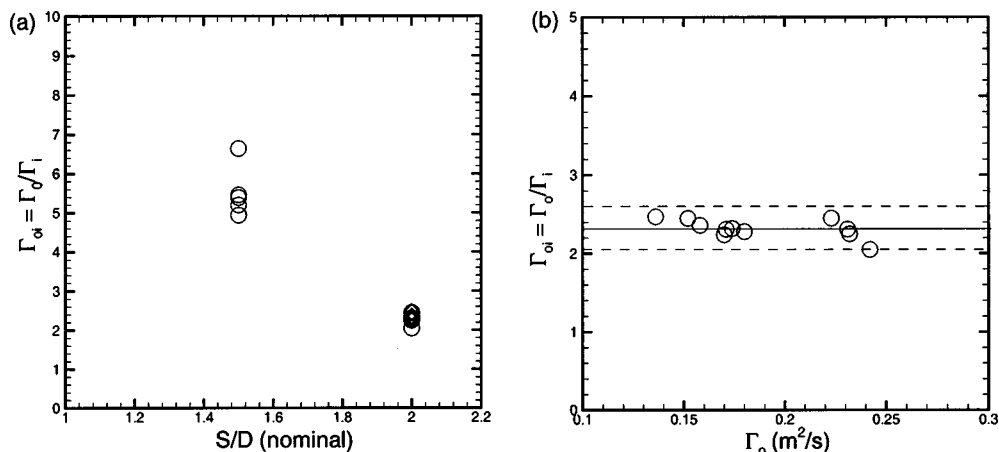


FIG. 18. Effect of SF_6 concentration on the relative strength of the outer and inner vortices. (a) Circulation ratio, Γ_o/Γ_i , vs nominal initial spacing, S/D , for both pure and diluted SF_6 cylinders. (○) Pure SF_6 ; (◇) SF_6 -air mix. (b) Circulation ratio, Γ_{oi} , vs outer vortex circulation, Γ_o , for all vortices at $S/D=2.0$. Mean is represented by solid line; dashed lines are the mean $\pm 12\%$.

18(b), in which Γ_{oi} is plotted against outer vortex strength, Γ_o . Figure 18(b) shows explicitly the variation, or lack thereof, in Γ_{oi} with Γ_o , and, by inference, with SF₆ concentration. Here we take advantage of the fact that Γ_o is approximately constant over all realizations and spacings for pure SF₆, and assume that any reduction in Γ_o relative to this “pure” level is due to decreased levels of SF₆ concentration. We further assume that Γ_o is proportional to the baroclinic vorticity deposition. The theoretical vorticity deposition estimates of Samtaney and Zabusky¹⁶ and Picone and Boris¹⁷ are then used to estimate the concentration of SF₆ in the cylinders that would yield our measured reduction in Γ_o . The lower bound for SF₆ concentration is calculated by taking the lowest value of Γ_o plotted, approximately 0.132 m²/s, and dividing it by the mean value for Γ_o at this spacing, 0.232 m²/s; this yields $\Gamma_{o,mix}/\Gamma_{o,pure}=0.57$. The theoretical estimates based on this value yield a concentration of SF₆ in the cylinders in the range 30%–40%. Assuming that the concentration is 35%, the corresponding range of Atwood number shown in Fig. 18(b) is $0.41 < A < 0.67$. Hence, this is the approximate range of A over which Γ_{oi} appears to be constant for $S/D=2.0$.

C. Vortex blob simulation

If our measurements of the vorticity field are accurate, and the hypothesis of TPRVB (that the variation in Γ_{oi} is strongly affecting the flow morphologies) is correct, then it should be possible to perform refined vortex blob simulations, based on the experimentally measured circulations, that will more closely reflect the experimental results. In Fig. 19, results are presented at late time for vortex blob simulations with $S/D=2.0$, 1.5, and 1.2. The morphologies in the left-hand column are computed with “ideal” baroclinic vorticity deposition, i.e., $\Gamma_{oi}=1.0$. The morphologies in the right-hand column are computed using the experimentally measured values of Γ_{oi} for each spacing. The initial conditions are included on each plot for clarity.

At each spacing, the flow morphologies based on the measured Γ_{oi} show excellent qualitative agreement with the morphologies observed experimentally. In Fig. 19(b), for example, each cylinder has evolved into a vortex pair with an angle of rotation and shape very similar to that seen in the experiment for $S/D=2.0$ (compare with Fig. 6(a) at late time). For $S/D=1.5$, see Fig. 19(d), the simulation leads to a dominant outer vortex, an apparent “disk” of dense gas representing the weak inner vortex, and a higher rate of rotation—a very similar pattern to that seen in Fig. 7(b) at late time. For the case of strong interaction, as seen in Fig. 19(f), the simulation also bears close resemblance to the experiment. The marker particles are induced around two dominant vortices, yielding a morphology much like that in Fig. 8(b), also with $S/D=1.2$. It should be noted that at early times, not presented here, there is slight disagreement between the simulations and experiment, even in the cases with measured Γ_{oi} . Specifically, a small cusp appears in the simulations along the material connecting the vortices. We suspect that this slight difference is due to a difference in the

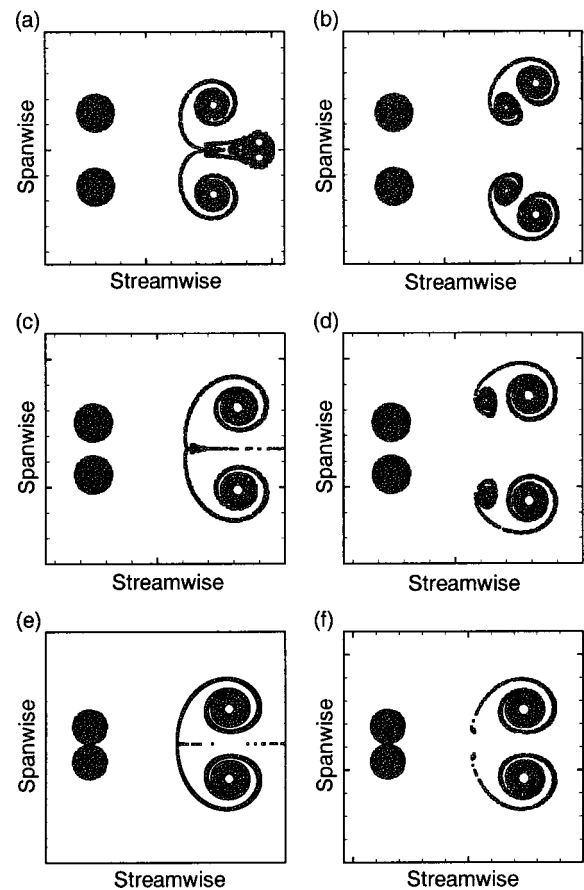


FIG. 19. Vortex blob simulations at late time with ideal and experimentally measured circulation ratio, $\Gamma_o/\Gamma_i=\Gamma_{oi}$, for three spacings. (a) Weak interaction, ideal case: $S/D=2.0$, $\Gamma_{oi}=1$. (b) Weak interaction, measured values: $S/D=2.0$, $\Gamma_{oi}=2.25$. (c) Moderate interaction, ideal case: $S/D=1.5$, $\Gamma_{oi}=1$. (d) Moderate interaction, measured values: $S/D=1.5$, $\Gamma_{oi}=5.5$. (e) Strong interaction, ideal case: $S/D=1.2$, $\Gamma_{oi}=1$. (f) Strong interaction, measured values: $S/D=1.2$, $\Gamma_{oi}=\infty$.

spatial extent of the deposited vorticity between the experiment and the idealized simulation.

In contrast, the simulations with “ideal” vorticity deposition result in morphologies that are qualitatively very different from those in the experiment. In each case, the inner vortices are mutually induced forward, as discussed in Sec. III (see the left-hand column of Fig. 19). As the cylinders are moved closer together, the induced velocity of the vortices increases, to the point in Fig. 19(e) where the inner vortices self-induce out of the field of view at early time and entrain only a few marker particles.

The high level of qualitative agreement between these vortex blob simulations and the experimentally observed morphologies provides indirect confirmation of the diagnostic and further support of the TPRVB hypothesis that the flow patterns are a result of weakened inner vortices. This agreement also suggests that the postshock flow evolution may be modeled reasonably well using incompressible, inviscid vortex dynamics.

VI. DECOMPOSITION AND STATISTICAL ANALYSIS OF INTENSITY FIELDS

It is desirable to distinguish those components of the flow field that are deterministic in nature from those that are

stochastic in nature. Many statistical procedures applied to steady flows, however, become inappropriate or difficult for transitional, e.g., shock-accelerated, flows. One important example of such a procedure is ensemble averaging. While clearly desirable for both qualitative and quantitative analysis, aspects of the current experiment make this analysis troublesome. One general issue is the sensitivity to initial conditions, discussed previously. A more specific issue is the presence of a slight timing jitter between the shock passing the pressure transducers and the firing of the lasers. This timing jitter leads to an effective spatial “jitter”—i.e., the structures will appear on the recording media at different spatial locations—that renders traditional ensemble averaging techniques inappropriate. In the present work, we use iterative correlation-based ensemble averaging (CBEA) to overcome these difficulties. This procedure extracts the persistent character of the structure, thereby obtaining a meaningful ensemble average, and permitting decomposition of the concentration field into mean and fluctuating components. For most spacings, we find that flow features at the large scales (scales 1 and 2, as defined earlier) and the intermediate scales (scale 3) are deterministic, while the small scales (scale 4) are stochastic.

A. Correlation-based ensemble averaging

In the CBEA procedure, the six dynamic exposures on each image are separated into individual image sections, so that there is one section per realization per time after shock impact. Then all of the sections for a given intercylinder spacing and time of exposure (typically around 15) are analyzed as a group to yield one ensemble-averaged result. These ensemble averages are then recombined to show the evolution of the average structure at a given spacing.

The analysis procedure is a template-matching scheme similar to that used by Soloff⁴⁴ to identify coherent structures in a turbulent pipe flow. A schematic of the procedure is presented in Fig. 20. In each case, one image section is selected as an initial intensity “template,” I_t , and matched to the remaining image sections at that spacing and time (intensity “fields,” I). The match is optimum in the sense that the mean square error between the field and the template,

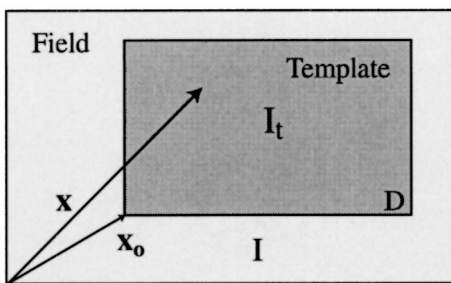


FIG. 20. Schematic of iterative correlation-based ensemble averaging (CBEA) procedure. A template, I_t , is matched to a field, I , by varying \mathbf{x}_0 to minimize the mean-square error between the two over the domain D . The region of optimum match is extracted, and used to create the next template or to form the final ensemble average.

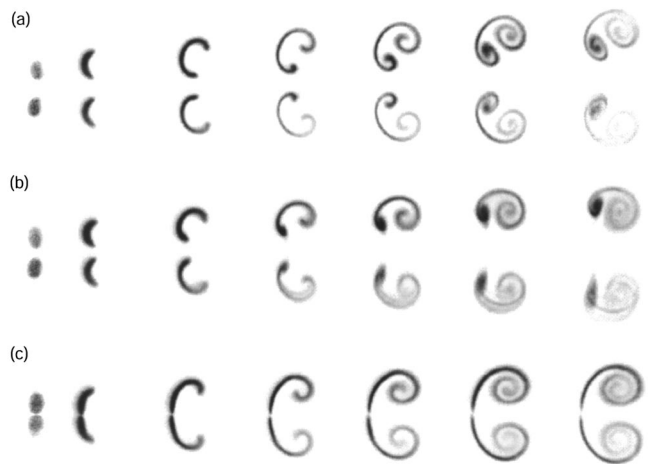


FIG. 21. Average concentration fields computed with correlation-based ensemble averaging (CBEA). (a) Weak interaction, $S/D=2.0$; (b) moderate interaction, $S/D=1.6$; (c) strong interaction, $S/D=1.2$.

$$e = \int_D (I(\mathbf{x}) - I_t(\mathbf{x} - \mathbf{x}_0))^2 dA, \tag{6}$$

is minimized over the domain D . This minimization requires maximization of the following correlation function:

$$R_{I_t} = \int_D I(\mathbf{x}) \cdot I_t(\mathbf{x} - \mathbf{x}_0) dA \tag{7}$$

with respect to the displacement vector, \mathbf{x}_0 . At this optimum \mathbf{x}_0 , the region $I(\mathbf{x} - \mathbf{x}_0)$ is extracted from the field. The extracted regions from all fields are then ensemble averaged in the traditional sense, yielding the conditional average $\langle I(\mathbf{x} - \mathbf{x}_0) | \mathbf{x}_0 \rangle$.

This result, derived directly from the images themselves, is then used as the template during a second iteration involving all of the image sections as fields. This second iteration produces the ensemble average. The iterative procedure minimizes dependence on the initial choice of template and converges quickly. Potential bias in the ensemble average due to slight variations in seeding density or laser pulse intensity from shot to shot are removed by a normalization procedure prior to analysis. Thus, CBEA yields one ensemble-averaged result (i.e., mean field) for each exposure time and cylinder spacing. An important advantage of the procedure is that the fluctuating fields are easily obtained by subtracting the ensemble-averaged field from each of the regions extracted from the original dynamic images (i.e., total fields).

Results from the CBEA procedure are presented in Fig. 21 for three values of S/D . As mentioned previously, each exposure is the result of one CBEA analysis, and the results at a given spacing are recombined for presentation. The average fields for the case of $S/D=2.0$ are shown in Fig. 21(a). Note that these average fields look qualitatively similar to the instantaneous fields given in Fig. 6(a). A significant amount of structure is observed to persist through the ensemble average; this includes the largest scales, associated with the cylinder separation and size (scales 1 and 2), and the intermediate scales, associated with each individual vortex (scale

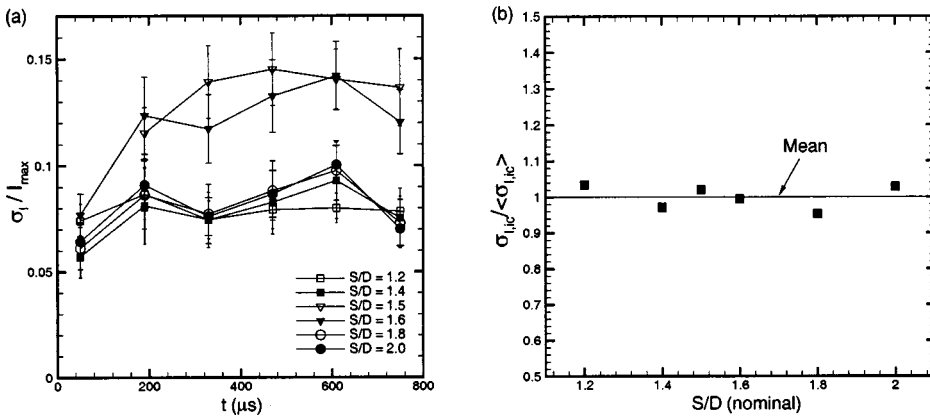


FIG. 22. Root-mean-square intensity, based on fluctuating intensity fields from CBEA decomposition. (a) Normalized rms intensity, σ_I / I_{\max} , vs time after shock passage, t , for all spacings. Error bars represent 95% confidence intervals. (b) Normalized root-mean-square intensity for initial condition images, $\sigma_{I,IC} / \langle \sigma_{I,IC} \rangle$, vs nominal initial spacing, S/D .

3). Differences between the total and average fields appear primarily in the smaller flow scales. For example, the waviness present along the air-SF₆ interface in the instantaneous fields (Figs. 6–8) at late time is not visible in the average fields; this absence is likely due to the fact that the phase of the secondary instability is random from shot-to-shot, and it is thus averaged out. The persistence of the large and intermediate scales through the average suggests that the CBEA procedure is effectively capturing the character of the flow morphologies. It also suggests, just as importantly, that the flow is deterministic on these scales—strong evidence of the repeatability of the experiment. Furthermore, the CBEA concentration fields for the other example of weak interaction, $S/D = 1.8$, are very similar, in terms of the structural level of detail.

The average structures for an example of strong interaction, $S/D = 1.2$, are seen in Fig. 21(c). While these morphologies are different from those in Fig. 21(a), they exhibit similar behavior in the sense that both the large and intermediate scales of the flow clearly emerge from the ensemble average. Additionally, the CBEA results from the other example of strong interaction ($S/D = 1.4$) are consistent with those shown here, again in terms of the level of structural detail and implications for experimental repeatability. As in Fig. 21(a), any manifestation of a secondary instability is averaged out, despite the clear appearance of waviness along the air-SF₆ interface in Fig. 8(b). As might be expected, these small-scale effects are more clear in the fluctuating fields; however, as mentioned previously, an investigation of small-scale activity is beyond the scope of the present work.

An unexpected result is that the high degree of repeatability seen in the above-given examples is not apparent in the spacings associated with moderate interaction. An example of average structures in this case is presented in Fig. 21(b), for $S/D = 1.6$. In this example, and in the data for $S/D = 1.5$, the images are characterized by a slight blurring, or smearing, of the structures, particularly at late time. Obviously, this blurring is not removed by the ensemble averaging procedure, and is thus a manifestation of alterations in the flow structures on certain scales. While one structure (the upper one) contains a relatively high level of detail, the other (lower) structure does not. This difference is a simple consequence of the CBEA procedure—the matching algorithm favors one cylinder over the other, and “locks on” to it, likely

due to slight differences in intensity between the cylinders. The implications of the resulting average field remain the same, of course, regardless of which cylinder is “locked on” to. Examination of the image suggests that the blurring is due to variations in the spacing between the two unstable cylinders (scale 1), and/or slight variations in the rotation rate. This relative increase in the variability of the moderate interaction case is consistent with the notion of a transition between two flow regimes occurring at $S/D \sim 1.5$.

B. rms fluctuating intensity

We investigate sensitivity to initial conditions by calculating the rms intensity fluctuations in the traditional sense. Here, the extracted intensity fields are used, i.e., those spatially registered with their associated ensemble-averaged field. Then the total intensity field, $I(x, y)$, is decomposed as $I(x, y) = \langle I(x, y) \rangle + I'(x, y)$, where $\langle I(x, y) \rangle$ is the ensemble-averaged intensity field and $I'(x, y)$ is the fluctuating intensity field. The rms fluctuating intensity, σ_I , is calculated as

$$\sigma_I = \left[\frac{\sum_x \sum_y (T(x, y) I(x, y) - T(x, y) \langle I(x, y) \rangle)^2}{N_p} \right]^{1/2}, \quad (8)$$

where the summations are carried out over all realizations. $T(x, y)$ is a thresholding indicator function given by

$$T(x, y) = \begin{cases} 1 & \text{if } I(x, y) + \langle I(x, y) \rangle \geq 2T_i \\ 0 & \text{if } I(x, y) + \langle I(x, y) \rangle < 2T_i, \end{cases} \quad (9)$$

and N_p is the total number of pixels considered, i.e., above the threshold. The threshold level, T_i , is set at 12% of the maximum intensity to eliminate any contribution, or false reduction, due to the consideration of regions of background noise.

The rms results are presented in Fig. 22. In Fig. 22(a), the normalized rms fluctuating intensity, σ_I / I_{\max} , is plotted as a function of time after shock passage, for all spacings considered. Here, the symbol shape corresponds to the data classification in terms of the degree of interaction (e.g., squares correspond to “strong” interaction, and so on). Error bars are also included for each point. The width of the line segments on the end of the bars is varied for each spacing, although the bars overlap because the images are obtained at the same times. These error bars represent the 95% confi-

dence intervals for our estimate of σ_I due to sampling error. The greatest uncertainty (interval) associated with any point is ± 0.018 .

The rms values for four of the spacings [$S/D = 1.2, 1.4, 1.8,$ and 2.0 , Fig. 22(a)] are quite consistent with one another. These curves start out at around $\sigma_I/I_{\max} = 0.06$, at the first dynamic pulse, and then increase slightly to $\sigma_I/I_{\max} \approx 0.08$; they remain at this approximate level for the duration of the realization, with some variation in time. At each time, however, the values of σ_I/I_{\max} for these four lower curves are very consistent, in the sense that the associated error bars overlap, often significantly. There appears to be a slight reduction in σ_I at the sixth dynamic pulse. This reduction may be an indication of the homogenization of the structure at late time. What is most significant in terms of the effects of the initial cylinder spacing on the structural evolution, however, is that for these four spacings the results are very consistent—and these are the spacings associated with the weak and strong interaction cases.

In contrast, the two curves associated with moderate interaction, $S/D = 1.5$ and 1.6 , exhibit quite different behavior. While at the first dynamic pulse, there is general agreement in the data, these curves show a sharp increase in σ_I at the second pulse. (Note that no value of σ_I is obtained at $t = 50 \mu\text{s}$ for $S/D = 1.5$, due to a reflection from the second dynamic pulse that overlaps the image from the first dynamic pulse at this spacing.) The difference between the moderate cases and the other cases becomes statistically significant at this time, in the sense that the error bars associated with the points do not overlap (though just barely). This difference persists for all later times measured, with σ_I values approximately 50% higher than those for all other spacings, and a clear separation of the associated error bars. Hence, the data suggest that the moderate interaction case is transitional between two flow regimes and thus less deterministic than the weak or strong cases, as it appeared from a qualitative examination of the ensemble-averaged morphologies.

We must ensure that the observed effects are not related to the initial conditions. A similar decomposition and rms analysis is performed on the initial condition images for each spacing. The results are presented in Fig. 22(b). Here, the IC normalized rms fluctuating intensity, $\sigma_{I,IC}/\langle\sigma_{I,IC}\rangle$, is plotted against S/D , where the brackets here denote an average over all spacings. It is clear from the figure that there is relatively little variation in $\sigma_{I,IC}$ with spacing, so the initial conditions are controlled equally well for all spacings. In particular, the two points associated with moderate interaction, $S/D = 1.5$ and 1.6 , are very close to the mean.

Thus, it appears that the statistically significant differences observed in Fig. 22(a) for the moderate interaction cases represent real differences in behavior between the initial spacings—specifically, a particularly keen sensitivity of the flow structures to the initial conditions for $S/D = 1.5$ and 1.6 . Also of interest is the fact that the deviation appears to occur not immediately, but between the first and second dynamic images. It may be the case that the effects of vortex induction are initially manifest during the second image.

VII. MECHANISMS OF INTERACTION

In the preceding sections, we have quantified the effects of cylinder–cylinder interaction on the postshock flow morphologies and the associated velocity/vorticity fields. The most apparent effect of this interaction, in terms of deviation from the single-cylinder case, is a severe weakening of the inner vortices. Vortex blob simulations have further demonstrated that such an alteration of the vorticity field at early time may lead to the observed flow morphologies. In this section, we outline and discuss four possible mechanisms by which this interaction may occur.

One possible type of interaction is vorticity cancellation or vortex annihilation between the inner vortices, which would take place after shock passage and the initial vorticity deposition. A second potential mechanism of interaction occurs during the passage of the shock wave through the double-cylinder configuration of dense gas. Such an interaction would affect the initial baroclinic vorticity deposition, in some way weakening the inner vortices relative to the outer ones. A third type of interaction might involve reflected shock waves that reverberate between the cylinders while they are in close proximity, i.e., immediately after shock passage (Cranfill,⁴⁵ Rider⁴⁶). A fourth potential interaction mechanism involves the oscillation (or propagation) of acoustic waves between (or through) the cylinders, during shock passage and at much later times.

The first mechanism, postshock vortex annihilation, could intuitively cause a severe alteration in the vorticity field; however, such a catastrophic annihilation would likely leave a strong footprint in the flowfield. For example, one would expect to see seemingly random, small-scale remnants of vorticity, but there is no evidence of these at late time. Furthermore, one would expect that such an interaction would be manifest in the flow morphologies, but this is not apparent either. The fourth mechanism (acoustic waves) may indeed be present in the system, but its greatest effect would likely be to create small-scale positive and negative contributions to the vorticity on both sides of existing density gradients. It seems unlikely that a series of acoustic waves would create a severe, large-scale net change in the vorticity field, like that observed experimentally. It seems most likely, then, that the strongest interaction occurs at early time, either during the initial shock passage (mechanism 2) or immediately thereafter via reflected shocks (mechanism 3).

Let us consider “mechanism 2” first. In this interpretation, the initial baroclinic vorticity deposited on the inner edges of the cylinders is less than that on the outer edges of the cylinders, and this vorticity distribution drives the flow evolution in rough accordance with incompressible vortex dynamics. This idea is consistent with the fact that the incompressible, idealized vortex blob simulations yield morphologies that are qualitatively very similar to those observed in the experiment. One key issue associated with this mechanism is: what happens during the shock passage to yield the weak inner vortices? One simple but feasible idea is that diffusion of the SF_6 is becoming important, and the cylinders begin to overlap at some concentration level, so that the baroclinic production is weaker for the inner structures.

Another possibility is that the shock undergoes complex distortions or refractions (e.g., shock focusing) that affect the (mis)alignment of the pressure and density gradients, and hence affect the baroclinic vorticity production.

The other likely interaction mechanism is via reflected shocks that reverberate between the cylinders immediately after the initial shock passage. In this model, the inner edges of the cylinders (and the associated inner blobs of deposited vorticity) would be subject to pressure gradients or waves distinct from those seen on the outer edges of the cylinders. Hence, the properties of the resulting inner vortices might be quite different from the outer structures, which is consistent with observations, although the exact mechanisms by which the inner vorticity is altered or destroyed are not clear.

VIII. SUMMARY AND CONCLUSIONS

We experimentally investigate the evolution and interaction of two shock-accelerated, RM-unstable gas cylinders. The cylinders are impacted by a planar, Mach-1.2 shock wave, and the initial spanwise separation of the cylinders is varied incrementally from $S/D = 1.2$ to 2.0. On each realization, concentration fields are visualized immediately before shock impact and at six times after shock impact by seeding the heavy gas with fog droplets. In a series of independent realizations, velocity (and vorticity) fields are obtained at one (late) time using particle image velocimetry; here, the heavy gas and carrier air are both seeded.

The morphologies of the unstable flow structures are observed to be highly sensitive to the initial cylinder spacing. The data sets are classified into groups, according to the observed degree of interaction between the cylinders (following TPRVB): weak ($S/D = 2.0$ and 1.8, $\Gamma_{oi} < 4$), moderate ($S/D = 1.6$ and 1.5, $4 < \Gamma_{oi} < 10$), and strong ($S/D = 1.4$ and 1.2, $\Gamma_{oi} \approx \infty$) interaction.

The effects of this interaction are quantified using both visualization and velocimetry. Several measures are introduced to quantify the large-scale concentration fields using principles of solid mechanics, including the “radius of intensity” as an estimate of mixing-zone width. Analysis reveals that the moderate interaction cases, in particular $S/D = 1.5$, exhibit the greatest rotation rate. It is hypothesized that this rotation is caused by a difference between the outer and inner vortex strengths. Measurements of the vorticity fields at late time show that, indeed, a principal effect of the interaction is to weaken the innermost vortices: the circulation of the outer vortices is observed to be independent of the cylinder spacing, while the inner vortices become weaker as the spacing is reduced. Furthermore, idealized vortex blob simulations based on the measured circulation ratio yield concentration morphologies that closely resemble the flow patterns observed experimentally.

An iterative, correlation-based, ensemble-averaging procedure successfully extracts the persistent character of the unstable flow structures, and permits decomposition of the concentration fields into mean (deterministic) and fluctuating (stochastic) components. The persistence of the large and intermediate scales through the average also provides strong evidence that the experiment is highly repeatable. While the

structures at all spacings are sensitive to the initial conditions, rms fluctuating intensity calculations reveal that the structures associated with the moderate interaction case have a particularly keen sensitivity to the ICs.

The present results do not permit conclusive quantification of the specific mechanisms of interaction. The above-presented body of data, however, is consistent with the hypothesis that the key cylinder–cylinder interaction occurs during the initial shock passage and baroclinic vorticity deposition.

ACKNOWLEDGMENTS

The authors would like to thank James Doyle, Norman Kurnit, Randall Johnson, Nagoor-Gani Mohamed, Michael Schneider, Cindy Zoldi for technical assistance, Charles Cranfill, James Kamm, and Cindy Zoldi for reviewing the manuscript, and the referees for their insightful remarks. This work was supported by DOE Contract No. W-7405-ENG-36 and Sandia Laboratories Grant No. BG-7553.

- ¹E. Meshkov, “Instability of the interface of two gases accelerated by a shock wave,” *Izv. Akad. Nauk SSSR, Mekh. Zhidk. Gaza* **4**, 151 (1969).
- ²R. D. Richtmyer, “Taylor instability in shock acceleration of compressible fluids,” *Commun. Pure Appl. Math.* **8**, 297 (1960).
- ³J. Lindl, R. McCrory, and E. Campbell, “Progress toward ignition and burn propagation in inertial confinement fusion,” *Phys. Today* **45** (9), 32 (1992).
- ⁴W. Arnett, J. Bahcall, R. Kirshner, and S. Woosley, “Supernova 1987A,” *Annu. Rev. Astron. Astrophys.* **27**, 629 (1989).
- ⁵J. Yang, T. Kubota, and E. E. Zukoski, “Applications of shock-induced mixing to supersonic combustion,” *AIAA J.* **31**, 854 (1993).
- ⁶J. Jacobs and J. Sheeley, “Experimental study of incompressible Richtmyer–Meshkov instability,” *Phys. Fluids* **8**, 405 (1996).
- ⁷M. Jones and J. Jacobs, “A membraneless experiment for the study of Richtmyer–Meshkov instability of a shock-accelerated gas,” *Phys. Fluids* **9**, 3078 (1997).
- ⁸O. Sadot, L. Erez, U. Alon, D. Oron, L. Levin, G. Erez, G. Ben-Dor, and D. Shvarts, “Study of nonlinear evolution of single-mode and two-bubble interaction under Richtmyer–Meshkov instability,” *Phys. Rev. Lett.* **80**, 1654 (1998).
- ⁹J. Jacobs, D. Jenkins, D. Klein, and R. Benjamin, “Nonlinear growth of the shock-accelerated instability of a thin fluid layer,” *J. Fluid Mech.* **295**, 23 (1995).
- ¹⁰P. Rightley, P. Vorobieff, and R. Benjamin, “Evolution of a shock-accelerated thin fluid layer,” *Phys. Fluids* **9**, 1770 (1997).
- ¹¹P. Rightley, P. Vorobieff, R. Martin, and R. Benjamin, “Experimental observations of the mixing transition in a shock-accelerated gas curtain,” *Phys. Fluids* **11**, 186 (1999).
- ¹²K. Prestridge, P. Rightley, P. Vorobieff, R. Benjamin, and N. Kurnit, “Simultaneous density-field visualization and PIV of a shock-accelerated gas curtain,” *Exp. Fluids* **29**, 339 (2000).
- ¹³K. Prestridge, P. Vorobieff, P. Rightley, and R. Benjamin, “Validation of an instability growth model using particle image velocimetry measurements,” *Phys. Rev. Lett.* **84**, 4353 (2000).
- ¹⁴M. Brouillette, “The Richtmyer–Meshkov instability,” *Annu. Rev. Fluid Mech.* **34**, 445 (2002).
- ¹⁵N. Zabusky, “Vortex paradigm for accelerated inhomogeneous flows: Viometrics for the Rayleigh–Taylor and Richtmyer–Meshkov environments,” *Annu. Rev. Fluid Mech.* **31**, 495 (1999).
- ¹⁶R. Samtaney and N. Zabusky, “Circulation deposition on shock-accelerated planar and curved density-stratified interfaces: Models and scaling laws,” *J. Fluid Mech.* **269**, 45 (1994).
- ¹⁷J. M. Picone and J. P. Boris, “Vorticity generation by shock propagation through bubbles in a gas,” *J. Fluid Mech.* **189**, 23 (1988).
- ¹⁸J. J. Quirk and S. Karni, “On the dynamics of a shock-bubble interaction,” *J. Fluid Mech.* **318**, 129 (1996).
- ¹⁹C. Zoldi, “A numerical and experimental study of a shock-accelerated

- heavy gas cylinder," Ph.D. thesis, Department of Applied Mathematics, State University of New York at Stony Brook, 2002.
- ²⁰J. F. Haas and B. Sturtevant, "Interaction of weak shock waves with cylindrical and spherical gas inhomogeneities," *J. Fluid Mech.* **181**, 41 (1987).
- ²¹J. Jacobs, "The dynamics of shock-accelerated light and heavy gas cylinders," *Phys. Fluids A* **5**, 2239 (1993).
- ²²K. Prestridge, C. Zoldi, P. Vorobieff, P. Rightley, and R. Benjamin, "Experiments and simulations of instabilities in a shock-accelerated gas cylinder," Los Alamos Technical Report No. LA-UR-00-3973, 2000.
- ²³A. Cook and P. Miller (private communication).
- ²⁴N. Zabusky (private communication).
- ²⁵M. Brouillette and B. Sturtevant, "Growth induced by multiple shock waves normally incident on plane gaseous surfaces," *Physica D* **37**, 248 (1989).
- ²⁶M. Brouillette and B. Sturtevant, "Experiments on the Richtmyer–Meshkov instability: Small-scale perturbations on a plane interface," *Phys. Fluids A* **5**, 916 (1993).
- ²⁷R. Bonazza and B. Sturtevant, "X-ray measurements of growth rates at a gas interface accelerated by shock waves," *Phys. Fluids* **8**, 2496 (1996).
- ²⁸J. Jacobs, D. Klein, D. Jenkins, and R. Benjamin, "Instability growth patterns of a shock-accelerated thin fluid layer," *Phys. Rev. Lett.* **70**, 583 (1993).
- ²⁹J. Budzinski, R. Benjamin, and J. Jacobs, "Influence of initial conditions on the flow patterns of a shock-accelerated thin fluid layer," *Phys. Fluids* **6**, 3510 (1994).
- ³⁰C. Tomkins, K. Prestridge, P. Rightley, P. Vorobieff, and R. Benjamin, "Flow morphologies of two shock-accelerated unstable gas cylinders," *J. Vis.* **5**, 273 (2002).
- ³¹R. J. Adrian, "Particle-imaging techniques for experimental fluid mechanics," *Annu. Rev. Fluid Mech.* **23**, 261 (1991).
- ³²C. E. Willert and M. Gharib, "Digital particle image velocimetry," *Exp. Fluids* **10**, 181 (1991).
- ³³I. Grant, "Particle-image velocimetry: A review," *Proc. Inst. Mech. Eng.* **211**, 55 (1997).
- ³⁴K. Christensen, S. Soloff, and R. Adrian, "PIV Sleuth: Integrated particle image velocimetry (PIV) interrogation/validation software," TAM Report No. 943, University of Illinois at Urbana–Champaign, 2000.
- ³⁵M. Raffel, C. Willert, and J. Kompenhans, *Particle Image Velocimetry: A Practical Guide* (Springer, Berlin, 1998).
- ³⁶C. D. Meinhart, A. K. Prasad, and R. J. Adrian, "A parallel digital processor for particle image velocimetry," *Meas. Sci. Technol.* **4**, 619 (1993).
- ³⁷A. K. Prasad, R. J. Adrian, C. C. Landreth, and P. W. Offutt, "Effect of resolution on the speed and accuracy of particle image velocimetry interrogation," *Exp. Fluids* **30**, 105 (1992).
- ³⁸J. Westerweel, "Efficient detection of spurious vectors in particle image velocimetry data," *Exp. Fluids* **16**, 236 (1994).
- ³⁹Y. Nakamura, A. Leonard, and P. Spalart, "Vortex simulation of an inviscid shear layer," AIAA Pap. No. 82-0948, AIAA/ASME Third Joint Thermophysics, Fluids, Plasma and Heat Transfer Conference, St. Louis, MO, 1982.
- ⁴⁰W. Rider (private communication).
- ⁴¹C. Zoldi (private communication).
- ⁴²R. J. Adrian, K. T. Christensen, and Z.-C. Lui, "Analysis and interpretation of instantaneous turbulent velocity fields," *Exp. Fluids* **29**, 275 (2000).
- ⁴³D. L. Reuss, R. J. Adrian, C. C. Landreth, D. T. French, and T. D. Fansler, "Instantaneous planar measurements of velocity and large-scale vorticity and strain rate using particle image velocimetry," SAE Paper No. 890616, 1989.
- ⁴⁴S. M. Soloff, "An investigation of the small-scale structure in a turbulent pipe flow using high resolution particle image velocimetry," M.S. thesis, Department of Theoretical and Applied Mechanics, University of Illinois at Urbana–Champaign, 1997.
- ⁴⁵C. Cranfill (private communication).
- ⁴⁶W. Rider (private communication).